ERCOFTAC workshop SIG47 – 3D Wakes
Imperial College London
10-11-12 April 2024

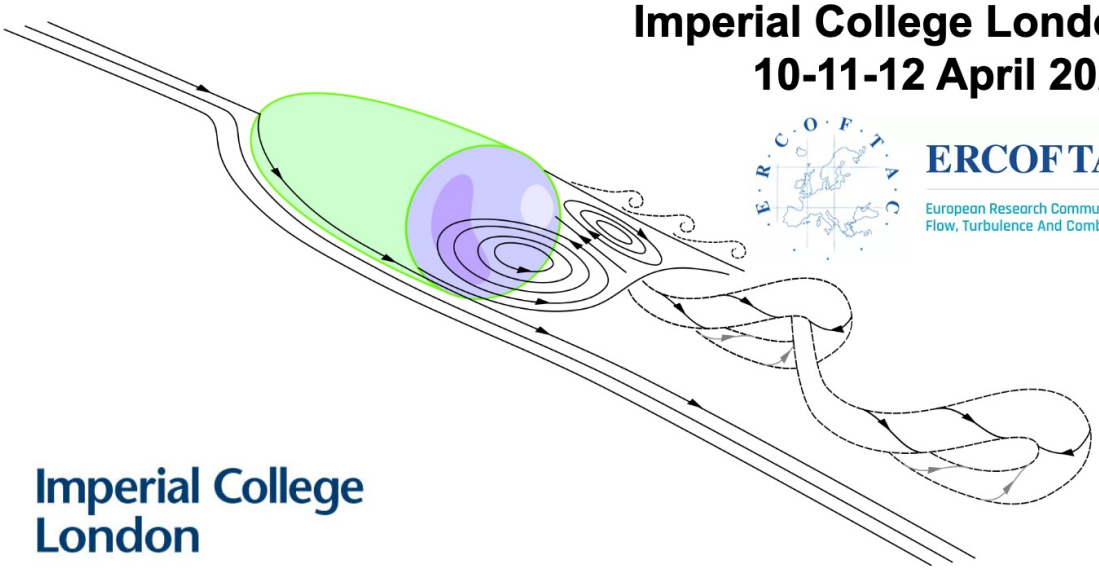

ERCOFTAC
European Research Community On Flow, Turbulence And Combustion

Imperial College London

Venue

Department of Aeronautics
City and Guilds Building
Imperial College

CAGB 300 (lecture theatre)
CAGB 309 (social)

Programme

Wednesday 10 April

13:45 – 14:00
Welcome and Introduction– Jonathan Morrison

14:00 – 15:00
Invited talk
Bérengère Podvin – *Low-order modelling of bistable dynamics: application to the case of an Ahmed body*

15:00 – 16:20
Session 1a: Wake dynamics – Chair Jonathan Morrison

Di Bao – *Effects of underflow perturbations on the wake and drag of three-dimensional bluff bodies*

Abhishek Mishra – *Effect of height on the wake recovery behind building clusters*

Guangyuan Huang – *Experimental and Numerical Investigations of Flow-Induced Noise from a D-Shaped Bluff Body in Ground Proximity*

Simran Singh Panesar – *Low frequency dynamics of the axisymmetric bluff body wake*

16:20 – 16:50
Break

16:50 – 17:50
Session 1b: Wake dynamics – Chair Jacques Borée

Samaresh Midya – *An experimental investigation of a high Reynolds number turbulent wake generated by a vehicle-like bluff body*

Wouter Terra – *The near wake of the generic cyclist model*

Marco Placidi – *Wake structure in urban areas*

Thursday 11 April

9:00 – 10:00
Invited talk
Edouard Boujo – *Stability and dynamics of the laminar wakes of 3D prisms*

10:00 – 11:20
Session 2: Stability and transition – Chair José I. Jiménez-González

Kacper Janczuk – *The effect of frontal geometry on 3D bluff body wakes*

Ivan Kharsansky Atallah – *Random switching dynamics and low frequency oscillations around airfoil stall*

Olivier Cadot – *Stochastic modelling of the wake reversal dynamics of a bluff body under different Reynolds numbers*

Lukasz Klotz – *Influence of porous material on the flow behind a backward-facing step - experimental study*

11:20 – 13:00
Lab tour

13:00 – 14:00
Lunch

14:00 – 15:00
Invited talk
Manuel Lorite-Díez – *Self-adaptive flaps for drag reduction in the Ahmed body wake*

14:00 – 16:00
Session 3a: Wake control – Chair Georgios Rigas

Tauha Khan – *Examination of mass flux equilibrium in the 3D turbulent wake of the flat-back Ahmed body using stacked stereoscopic PIV*

José M. Camacho-Sánchez – *On the role of blowing configuration for efficient drag Reduction of a 3d blunt body*

Pedro Solis – *Experimental passive control of the Ahmed body without ground effect using deflectors at a low Reynolds number*

16:00 – 16:30
Break

16:30 – 17:30
Session 3b: Wake control – Chair Olivier Cadot

J.C. Muñoz-Hervás – *Exploring wake dynamics interaction with rear flexible Flaps on a squareback ahmed body*

Manuel Garrido-Martin – *Exploring the effects of spanwise wing deformation on lift coefficient and trailing vortices properties at low Reynolds number*

Quentin Martinez – *Stall Flutter Characteristics of a Pitching NACA 63(3)418 Aerofoil with Passive Camber Morphing Capabilities*

19:00-23:00

Buffet supper at Builder's Arms Pub
1 Kensington Court Place W8 5BJ
At participant's own cost
(10 min walk - see map below)

Friday 12 April

9:00 – 10:00

Invited talk

Georgios Rigas – *Reinforcement learning of active aerodynamics in wind tunnel environments*

10:00 – 11:00

Session 3: AI and optimisation – Chair Aimee Morgans

Agostino Cembalo – *From on-road experiments to active closed loop control of base drag variations for slowly varying upstream flow conditions.*

Yajun Fan – *Optimised drag configurations of an Ahmed body in crossflow with top and bottom rear morphing spoilers allowing twisted deformations*

Yusuf Patel – *Reconstruction of turbulent bluff body wake using Physics Informed Neural Networks*

11:00 – 11:30

Break

11:30 – 12:30

Discussion about the ERCOFTAC SIG47 "3D Wakes" – Chair Jonathan Morrison and Olivier Cadot

12:30 – 13:30

Lunch & close

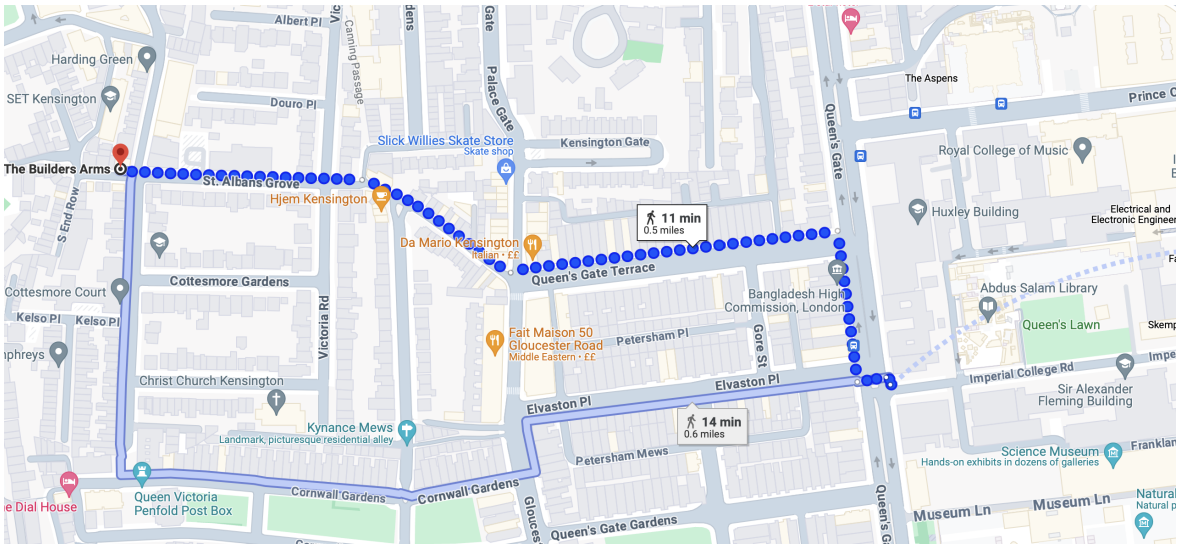

Figure 1: Supper Venue: Thursday, April 11, 19:00-23:00 Builder's Arms Pub (left)

Low-order modelling of bistable dynamics: application to the case of an Ahmed body

Bérengère Podvin* Stéphanie Pellerin †Yann Fraigneau ‡

Under certain conditions, the wakes behind bluff bodies representative of road vehicles are characterized by apparently spontaneous switches between quasi-steady reflection-breaking states [1]. The typical time separating switches is several orders of magnitude larger than the convective time scale, which makes them difficult to track in numerical simulations [2]. Understanding the physics of the switches and modelling their statistics [3] is of direct engineering interest as these asymmetric states have been shown to correspond to a higher pressure drag. However, such modelling approaches are also relevant for a wide class of turbulent flows for which multistability appears to be a generic feature, such as Rayleigh-Bénard convection [4] or flow interaction with a pendulum [5].

We describe a general framework in which a hierarchy of models can be constructed to capture the flow dynamics. The models are derived by projecting the Navier-Stokes equations onto a basis of modes obtained through application of Proper Orthogonal Decomposition (POD). Closure of the equations is performed using a modified eddy viscosity hypothesis where the dissipation parameters are determined from the identified quasi-steady states [6].

The procedure was applied to the direct numerical simulation of the flow around a squareback Ahmed body at a moderate Reynolds number (see figure 1). The dataset from which the modes are extracted was artificially enlarged to satisfy the statistical symmetries of the flow [7]. Switches in the main deviation of the wake were found to be associated with a specific spatial POD mode, termed the switch mode, which corresponded to faster flow on the upper side of the wake, and slower flow on its lower side. A six-mode model was able to display wake switching dynamics in the absence of noise, and to reproduce more closely the features of the switches when noise was added into the equations. The onset of the switches in the model was shown to coincide with the activation of the switch mode and with an increase in the intensity of POD modes corresponding to vortex shedding [8], as shown in figure 2.

POD modes were also found to be relevant to describe the connection between pressure and velocity fluctuations in the near wake. It was shown that the dominant pressure modes could be correctly estimated from the velocity field. Conversely the switch and deviation modes could be recovered directly from the pressure, which was not the case for the vortex shedding modes [9]. These findings raise the possibility that the models could be used as low-cost surrogates to estimate or predict broad changes in the flow dynamics.

References

[1] M. Grandemange, O. Cadot, and M. Gohlke. Reflectional symmetry breaking of the separated flow over three-dimensional bodies. *Physical Review E*, 86(3):035302, 2012.

[2] O. Evsafyeva, A. Morgans, and L. Dalla Longa. Simulation and feedback control of the ahmed body flow exhibiting symmetry breaking behaviour. *J. Fluid Mech.*, 817, 2017.

[3] G. Rigas, A.S Morgans, R.D. Brackston, and J.F. Morrison. Diffusive dynamics and stochastic models of turbulent axisymmetric wakes. *J. Fluid Mech.*, 778(R2), 2015.

[4] Qi Wang, David Goluskin, and Detlef Lohse. Lifetimes of metastable windy states in two-dimensional rayleigh–bénard convection with stress-free boundaries. *Journal of Fluid Mechanics*, 976:R2, 2023.

[5] Ariane Gayout, Mickaël Bourgoin, and Nicolas Plihon. Rare event-triggered transitions in aerodynamic bifurcation. *Phys. Rev. Lett.*, 126:104501, Mar 2021.

*Université Paris-Saclay, CNRS, CentraleSupélec, Laboratoire EM2C, 91190, Gif-sur-Yvette, France
†Université Paris-Saclay, CNRS, Laboratoire interdisciplinaire des sciences du numérique, 91405, Orsay, France
‡Université Paris-Saclay, CNRS, Laboratoire interdisciplinaire des sciences du numérique, 91405, Orsay, France

[6] B. Podvin and A. Sergent. Precursor for wind reversal in a square rayleigh-bénard cell. *Physical Review E*, 05(1):013112, 2017.

[7] B. Podvin, S. Pellerin, Y. Fraigneau, A. Evrard, and O. Cadot. Proper orthogonal decomposition analysis and modelling of the wake deviation behind a squareback ahmed body. *Phys. Rev. Fluids.*, 6(5):064612, 2020.

[8] B. Podvin, S. Pellerin, Y. Fraigneau, G. Bonnavion, and O. Cadot. Low-order modelling of the wake dynamics of an ahmed body. *J. Fluid Mechanics*, 927:R6, 2021.

[9] Bérengère Podvin, Stéphanie Pellerin, Yann Fraigneau, Guillaume Bonnavion, and Olivier Cadot. Relationship between the base pressure and the velocity in the near-wake of an ahmed body. *Phys. Rev. Fluids*, 7:054602, May 2022.

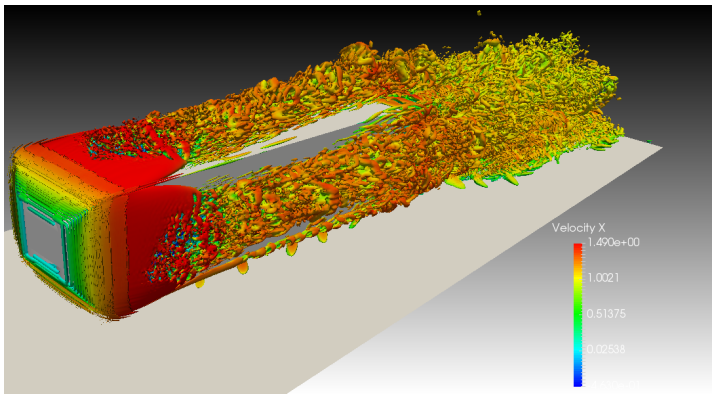

Figure 1: Instantaneous snapshot of the flow behind the Ahmed body for a Reynolds number of $Re = 10^4$ - Isosurface of Q criterion colored by streamwise velocity

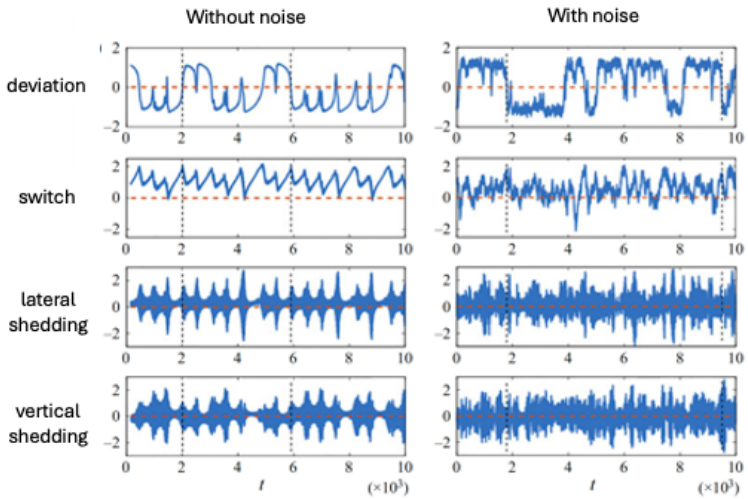

Figure 2: Time series of POD modes integrated with the low-dimensional model - adapted from [8]

Effects of underflow perturbations on the wake and drag of three-dimensional bluff bodies

D. Bao[1], J. Borée[1], C. Sicot[1] and C. Robroeck[2],

[1] *Institut Pprime, UPR-3346 CNRS – ISAE-ENSMA – Université de Poitiers, Futuroscope Chasseneuil, France.*
[2] *MFP Michelin, Site de LADOUX, Clermont-Ferrand, France.*
https://www.imperial.ac.uk/aeronautics/ercoftac/

10-12 April 2024

Abstract

The impact of underflow perturbations on the wake and aerodynamic drag of fast- and square-back bluff bodies is investigated. A pair of D-shaped obstacles is placed under the bodies and the relative distance l between the obstacles and the body base is varied. For both bodies, we reveal two successive drag-sensitive regimes for $l/d < 2.5$ (d is the obstacle width). In these regimes, we find that a mean mass transfer from the body wake to the obstacle wakes is responsible for a base drag increase of up to 16% and is not sensitive to the body shape. Finally, the differences in the influence of the obstacles between these two bodies are discussed.

1 Introduction

The wheels themselves and their interactions with the main body of a vehicle are responsible for more than 25% of the aerodynamic drag [1]. Therefore, the wheel-vehicle aerodynamic interaction problem is one of the major factors to be considered during the aerodynamic optimization process.

The nature of wheel-vehicle aerodynamic interaction was studied in [2] with a basic question: what are the salient features of the flow perturbations induced by wheels that drive this interaction? Starting from rotating/stationary wheels having representative deformable tires [3], it was shown that the momentum deficit created in the underflow by the wheels, in particular the rear wheels, is an important enabler to this interaction. At first order, it is therefore believed that wheels can be seen as underbody perturbations and that the key aerodynamic features are the underflow blockage, the wheel-wake development in the underflow and its interaction with the near wake of the vehicle.

Following the preliminary tests carried out in [2], our choice has been to use a Windsor body [4] and to perturb the wake of this geometry by placing, in the underflow, a pair of streamlined "D-shaped" obstacles of varying width. The two obstacles are mounted at varying relative distances from the vertical base of the body. The back shape of the Windsor body is varied in order to generalize the findings to different vehicle geometries and to similar flow situations. Our goal is first to analyze how the main wake of the body is modified by the wakes of these obstacles, of much smaller size, developing along the underflow. The final goal is to understand the flow mechanisms responsible for the significant drag and lift changes with varying obstacle-to-base distance found in [2].

2 Experimental setup

The experimental setup is shown in figure Figure (1). Two Windsor bodies are considered as shown in figure Figure (1)(a). The fast-back (square-back) Windsor body with height $H = 0.289$ m, width $W = 0.389$ m and length $L = 0.986$ m (1.147 m) is placed on a raised floor in the S620 closed-loop wind tunnel at ENSMA with a ground clearance of $G = 50$ mm. The length of the slanted base L_f having an angle of $\alpha = 20°$ is 0.222 m. A free-stream velocity $U_0 = 25\ m/s$ is considered, corresponding to a height-based Reynolds number $Re_H = 4.8 \times 10^5$. The pressure on the base surfaces is monitored by several pressure taps (shown in figure Figure (1)(b) by points) connected to a pressure scanner. Two differential pressure sensors (denoted by circles in figure Figure (1)(b)) are additionally used for time-resolved measurements. The velocity fields in the near-wake are measured by a PIV (Particle image velocimetry) system over two FOVs (fields of view) as depicted in figure Figure (1)(c). They are respectively located in the symmetry plane of the model ($y/H = 0$), and in a cross-flow plane in proximity to the base ($x/H = 0.03$). Two-component (2D2C) and stereoscopic (2D3C) PIV set-ups are respectively used for the first FOV and the second FOV.

The obstacles are of half-elliptic shape. Their length equal to one and a half times the width d. The width and height of the obstacles are $d/H = 0.19$ and $h/H = 0.17$, respectively. The height generates two $\delta = G - h$ =1.5 mm gaps between the body and the obstacles which are carefully filled with high-density foams. The relative distance from the base of the obstacle to the base of the body is l, which ranges from 0 d (flush-mounted to the base) to 5 d.

3 Results and discussion

The base drag C_B is defined as the opposite of the space-averaged pressure coefficient on the base surfaces. For the fast-back configuration, the slanted angle is taken into account for the calculation. The variations of the mean base drag $\Delta\overline{C_B} = \overline{C_B} - \overline{C_{B0}}$ with the obstacle-to-base distance l/d are shown in figure Figure (2)(a) for both configurations. The subscript 0 denotes the unperturbed baseline case ($\overline{C_{B0}} = 0.197$ for fast-back and $\overline{C_{B0}} = 0.188$ for square-back). For representative cases, the distributions of mean base pressure difference $\Delta\overline{C_p} = \overline{C_p} - \overline{C_{p0}}$ are shown.

First of all, a major difference between the fast-back and the square-back configurations is noticed. When the

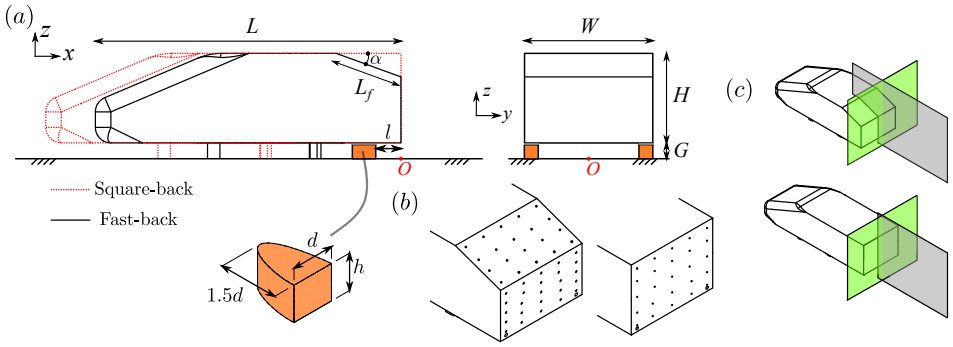

Figure 1: Experimental set-up. (a) Arrangement of the model above a raised floor, a detailed picture of the obstacle is inserted. (b) Locations of pressure taps on the base surfaces. (c) Positions of the particle image velocimetry fields of view.

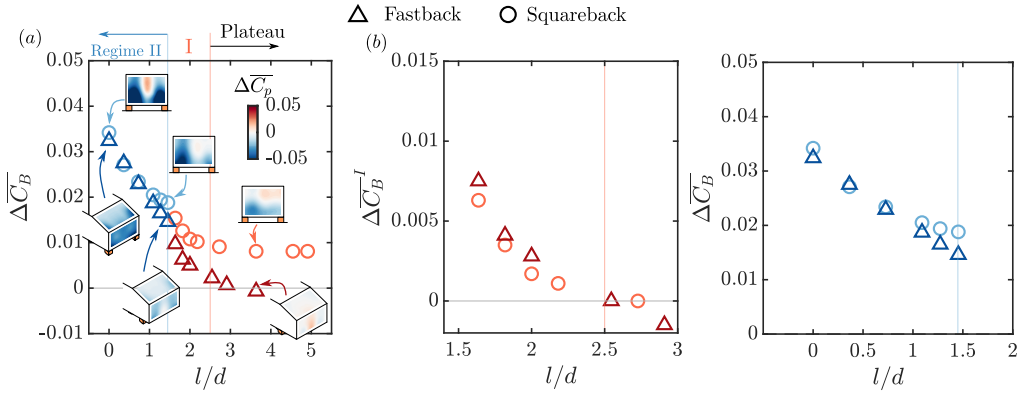

Figure 2: (a) Base drag of the body $\Delta\overline{C_B} = \overline{C_B} - \overline{C_{B0}}$ as a function of the obstacle-to-base distance l/d. ($b - c$) Comparison of base drag changes in regime I (b) and regime II (c).

obstacles are placed the most upstream of the base at the maximum l/d, no obvious change in the base drag is measured for the fast-back. By looking at the pressure distribution on the base surfaces, we notice that there is a modification of the vertical wake balance for the square-back configuration at $l/d \approx 4$ but not for the fast-back configuration. This means that the wake balance of the fast-back model is less sensitive to this type of perturbation in the underflow.

Nevertheless, the trends of these two configurations are very similar. Moving the obstacles from the most upstream position (maximum l/d) towards the base with decreasing l/d, a slight increase in base drag is noticed before $l/d = 2.5$. From $l/d = 2.5$ to 0 with reducing obstacle-to-base distance, a rapid increase in base drag is noticed. Maximally, we measure a base drag increase of $\Delta\overline{C_B}/\overline{C_{B0}} \approx 16\%$. By looking at the fluctuating pressure and velocity signals behind the obstacles (not shown here for brevity), two drag-sensitive regimes are defined for both configurations. In regime I ($1.5 < l/d < 2.5$) and the plateau, signatures of Kármán vortex shedding are noticed behind the obstacles. In regime II ($0 < l/d < 1.5$), these signatures are suppressed.

By defining a base drag variant $\Delta\overline{C_B}^I = \overline{C_B} - \overline{C_B}(l/d = 2.5)$, we notice in figure Figure (2)(b) that the level of base drag increase in regime I from the plateau is not varied by the shape of the body. Moreover, in regime II, the base drag increase $\Delta\overline{C_B}$ is measured to be only slightly modified.

Detailed pressure and velocity measurements not presented here for brevity, show that the sharp base drag increases are driven by a mean mass transfer from the main body wake to the wakes of the obstacles. This phenomenon is insensitive to the change in back shape of the body. On the other hand, the vertical wake balance of the square-back body is found to be more sensitive to the presence of obstacles than that of the fast-back body. These detailed results along with a physical model will be proposed and discussed at the conference in order to explain why the strong interaction regimes are insensitive to the shape of the body. These results can be also found in our previous published papers [5, 6]. A more applied situation with the use of rotating wheels is considered to validate the present findings [7]. We believe that the mechanisms we have uncovered also govern similar flow configurations, as seen in offshore facilities and civil structures.

References

[1] G. Wickern, K. Zwicker, and M. Pfadenhauer. Technical Report 970133, Society of Automotive Engineers, Inc., 1997.

[2] Y. Wang. *Experimental study of wheel-vehicle aerodynamic interactions.* PhD thesis, Chasseneuil-du-Poitou, ENSMA, 2019.

[3] Y. Wang, C. Sicot, J. Borée, and M. Grandemange. *J. Wind Eng. Ind. Aerodyn.*, 198:104062, 2020.

[4] G. Pavia, M.A. Passmore, M. Varney, and G. Hodgson. *J. Fluid Mech.*, 888:A33, 2020.

[5] D. Bao, J. Borée, Y. Haffner, and C. Sicot. *J. Fluid Mech.*, 936:A2, 2022.

[6] D. Bao, J. Borée, C. Sicot, and C. Roebroeck. *Accepted for publication in Exp. Fluids*, 2024.

[7] D. Bao, J. Borée, C. Sicot, and C. Roebroeck. *J. Wind Eng. Ind. Aerodyn.*, 236:105366, 2023.

EFFECT OF HEIGHT ON THE WAKE RECOVERY BEHIND BUILDING CLUSTERS

Abhishek Mishra, Marco Placidi, Matteo Carpentieri, Alan Robins
Centre of Aerodynamics and Environmental Flow, University of Surrey, Guildford GU2 7XH, UK

To accommodate the growing population, tall buildings are being erected both in clusters and in isolation. These buildings obstruct the atmospheric flows resulting in a significant impact on wind comfort for pedestrians, surface temperatures, and dispersion of pollutants [1-3]. The height of the buildings plays a pivotal role in interacting with atmospheric flows. Studies have shown that tall buildings have a greater impact on the growth of the rooftop shear layer [4]. These tall buildings are also observed to affect aerodynamic properties such as drag [5, 6]. The wake analysis of tall building clusters is complicated due to the existence of different wake regimes, each with distinct flow characteristics [7].

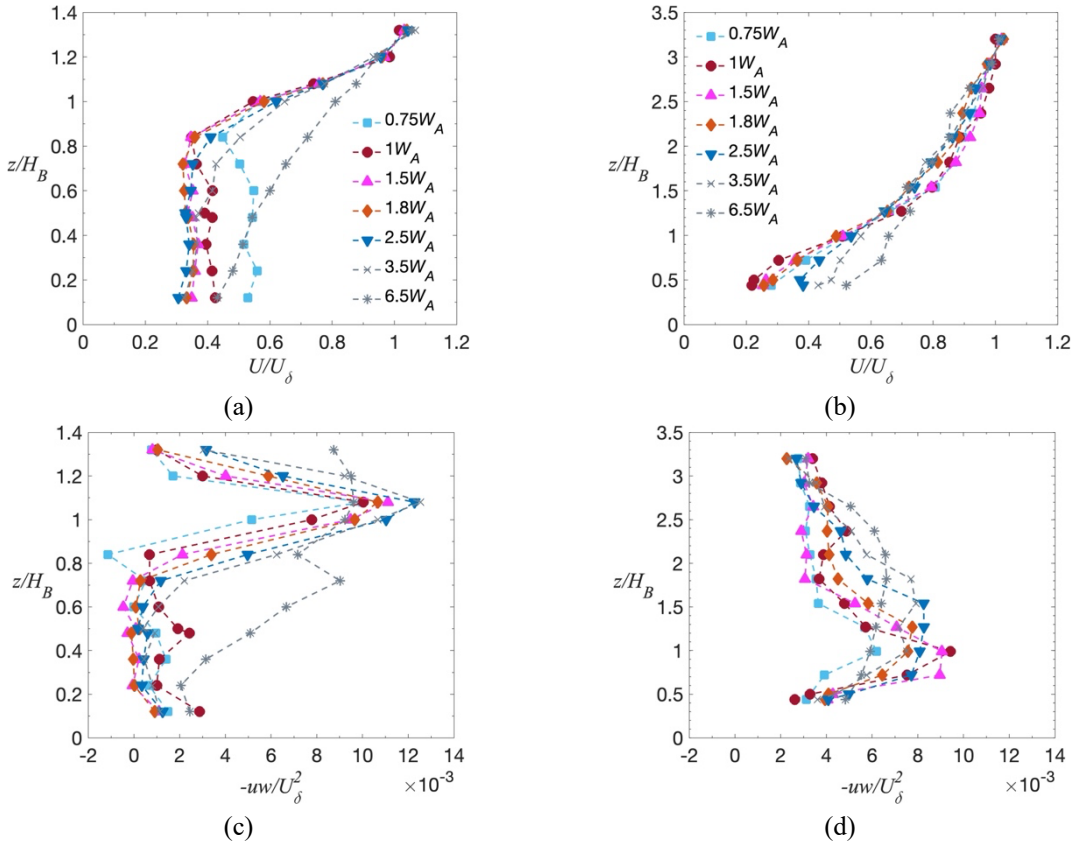

Figure 1: Vertical variation of mean velocity profiles (a, b) and momentum flux (c, d) for a 4X4 building cluster of height (H_B) = 500 mm (a, c) and 125 mm (b, d)

In this talk, we will discuss the effect of cluster height (H_B) on the development and recovery of the wake behind a cluster of buildings regularly arranged in a 4X4 array in the direction of the wind. Results show that with an increase in H_B, the boundary layer flow recovers more slowly to its undisturbed state, resulting in a zone of uniform-momentum flow, where the vertical gradient of the velocity is negligible (Figure 1a, b). Due to this, the vertical momentum exchange is suppressed in a certain region for tall building clusters (Figure 1c) when compared to clusters comprising shorter buildings (Figure 1d). This is expected to have a greater impact on the dispersion of pollutants around tall buildings. Several other cluster characteristics will be discussed during the talk.

References

[1] Xu, X., Yang, Q., Yoshida, A., & Tamura, Y. (2017). Characteristics of pedestrian-level wind around super-tall buildings with various configurations. *Journal of Wind Engineering and Industrial Aerodynamics*, *166*, 61-73.

[2] Li, Y., Schubert, S., Kropp, J. P., & Rybski, D. (2020). On the influence of density and morphology on the Urban Heat Island intensity, Nat. Commun., 11, 2647.

[3] Marucci, D., & Carpentieri, M. (2020). Dispersion in an array of buildings in stable and convective atmospheric conditions. *Atmospheric environment*, *222*, 117100.

[4] Lim, H. D., Hertwig, D., Grylls, T., Gough, H., Reeuwijk, M. V., Grimmond, S., & Vanderwel, C. (2022). Pollutant dispersion by tall buildings: Laboratory experiments and Large-Eddy Simulation. *Experiments in Fluids*, *63*(6), 92.

[5] Cheng, W. C., & Yang, Y. (2023). Scaling of flows over realistic urban geometries: A large-eddy simulation study. *Boundary-Layer Meteorology*, *186*(1), 125-144.

[6] Sützl, B. S., Rooney, G. G., & van Reeuwijk, M. (2021). Drag distribution in idealized heterogeneous urban environments. *Boundary-Layer Meteorology*, *178*(2), 225-248.

[7] Mishra, A., Placidi, M., Carpentieri, M., & Robins, A. (2023). Wake Characterization of Building Clusters Immersed in Deep Boundary Layers. *Boundary-Layer Meteorology*, *189*(1), 163-187.

Experimental and Numerical Investigations of Flow-Induced Noise from a D-Shaped Bluff Body in Ground Proximity

Guangyuan Huang*[1] and Zhigang Yang[2]

[1]Centre for Aeronautics, Cranfield University, Cranfield, United Kingdom, MK43 0AL
[2]Shanghai Automotive Wind Tunnel Center, Tongji University, Shanghai, PR China, 201804

March 18, 2024

Abstract

Flow-induced noise of bluff bodies has been a popular topic among research of bluff-body flows. When a bluff body is placed in proximity to a solid wall, its flow features can become complicated with a three-dimensional (3-D) and less coherent wake. Correspondingly, the flow-induced noise is expected to change. In this work, flow and the induced noise of a D-shaped bluff body in ground proximity is investigated experimentally and numerically. This body, which was employed in amount of previous works, is an elongated bluff cylinder with its profile resembling a straight-back Ahmed body's cross-section. The gap-to-height ratio is fixed at $G/H = 0.2$ in this study and height-based Reynolds number of the flow is prescribed as $Re_H = 23,000$. Experimental measurements were conducted in a closed-circuit wind tunnel with implementations of particle image visualisation, hot-wire velocimetry and surface oil visualisation. Moreover, direct aeroacoustic simulations were performed by solving compressible Navier-Stokes equations, as well as validated against the experimental results. Results show the flow is characterized by a leading-edge separation and reattachment over the body's upper side, massive separations from trailing edges, and a 3-D wake with intermittent vortex shedding. The acoustic far-field presents direcitvity of sound pressure in vertical and upstream directions. Significant tonal noise is captured at higher frequencies over the vortex-shedding frequency. Further discussions are made about the noise generation and propagation processes.

1 Introduction

Flow-induced noise of bluff bodies has been a popular topic among research of bluff-body flow, as it underpins fundamental fluid mechanics as well as practical engineering applications. Similarly, the effect of ground proximity on bluff body flow has received intensive attentions. Although there have been numerous studies on the flow-induced noise and the ground effect, to authors' knowledge, the inter-discipline of these two fields has not been thoroughly investigated. Therefore, this work focus on the flow-induced noise from a bluff body in ground proximity.

This work employs a D-shaped elongated bluff cylinder, which has been popularly used in previous aerodynamic research at sub-critical Reynolds numbers. Flow around the body in free space is characterized by early separations over its leading edges and approximately two-dimensional vortex shedding in its massive wake [Pastoor et al., 2008, Krajnović and Fernandes, 2011, Parkin et al., 2014]. Significant pressure waves are generated by the vortex shedding and propagates as an acoustic dipole in the lift direction [Huang et al., 2022]. When the body is placed proximity to a moving ground with a gap-to-height ratio of 0.2, the vortex shedding is greatly attenuated and the wake shows little coherence [Parkin et al., 2015].

In this work, flow and the induced noise of the D-shaped body in proximity to a stationery ground are investigated. Experimental investigation is conducted by wind tunnel measurements, followed by high-fidelity modelling using direct aeroacoustic simulations.

2 Experimental and Numerical Methods

2.1 Wind tunnel testbed

The experiments are conducted in a closed-circuit wind tunnel at Shanghai Automotive Wind Tunnel Center. The wind tunnel consists of a closed test section, whose dimensions are $556 \times 333 \times 2000$ mm in width, height, and length, respectively. The maximum flow speed of the wind tunnel is 44 m/s and turbulence intensity is lower than 0.22% at a flow speed of 11 m/s. Further information about the wind tunnel specifications is available in [Huang et al., 2022].

The D-shaped body is mounted vertically in the test section, as shown in Figure 1, spanning all the test section height. The dimensions of the D-shaped body are $L = 109.2$ mm, $H = 30$ mm, $W = 333$ mm in chord length, body height, and spanwise width, respectively. The corresponding span-to-height ratio is $W/H = 11.1$ to ensure the flow over body's middle section being little influenced by ending effects. An additional plane is placed parallel to

*Email: guangyuan.huang@cranfield.ac.uk

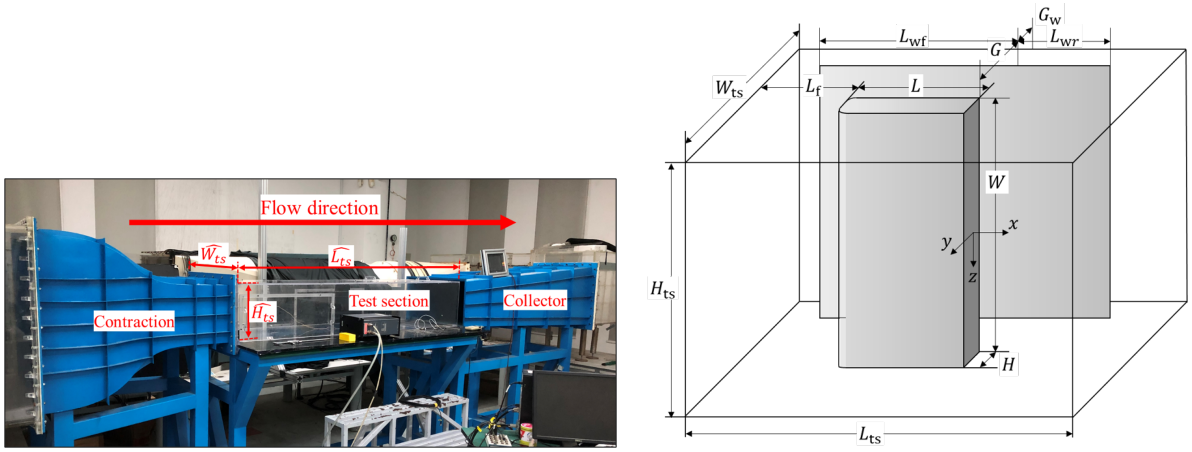

(a) Wind tunnel layouts (b) Experimental setup

Figure 1: Demonstrations of the wind tunnel layout and the experimental setup.

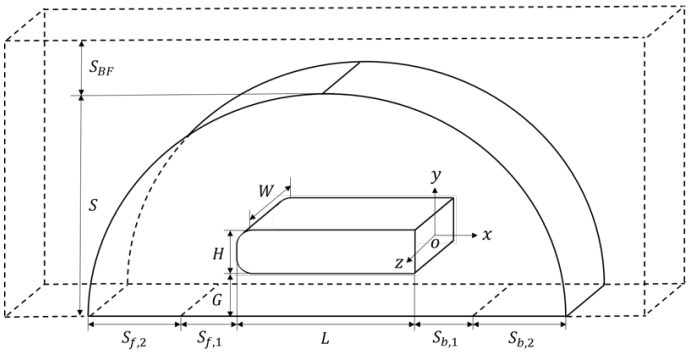

Figure 2: Schematics of the computational domain and numerical setup (dimensions not to scale).

the body to approximate a stationery ground. The plane has a length of 700 mm and spans all the wind tunnel height as well. The gap between the plane and the body's lower side is $G = 6$ mm, leading to a gap-to-height ratio of $G/H = 0.2$. The plane's leading edge is streamlined and $L_{\text{wf}} = 120.8$ mm distant from the body's rear surface in streamwise direction to ensure a thin boundary layer over the ground. The real blockage ratio of the body is resulted as 5.86% and, thus, freestream velocity is adjusted based on a blockage correction method purposed by Cowdrey [Cowdrey, 1968]. Reynolds number is defined in terms of the body height H and the adjusted freestream velocity U_∞ as $Re_H = U_\infty H/\nu$, where ν denotes the kinematic viscosity. All experiments are performed at $Re_H = 2.3 \times 10^4$ within a room temperature of 20 ± 0.2 °C.

A DANTEC one-dimensional hotwire velocimetry system is utilized to record the time history of instantaneous velocity amplitude in the boundary layer and the wake. A two-dimensional particle image velocimeter (PIV) system is employed to capture snapshots of the instantaneous velocity field. The laser generator and the camera are synchronized by a TSI laser-pulse synchronizer to enable so-called "double-frame/single-exposure" recording. The interrogation window size is set as 32×32 pixels, corresponding to a physical size at 1.85×1.85 mm^2. In addition, surface oil flow visualization is conducted to capture time-averaged surface flow features.

2.2 Direct aeroacoustic simulation

Direct aeroacosutic simulations (DAS) are conducted using a general-purpose Computational Fluid Dynamics solver ANSYS Fluent 2020R2. Monotonically Integrated Large Eddy Simulation (MILES) is employed to model the flow turbulence and the acoustics is obtained simultaneously within the compressible flow solutions. Further information about DAS implementation in ANSYS Fluent was described in [Huang et al., 2021].

Hereafter, all quantities are dimensionless, which are normalized by reference length H, velocity U_∞, density ρ_∞, and pressure $\rho_\infty {U_\infty}^2$. Figure 2 demonstrates the computational domain. The D-shaped body is placed in a half cylindrical physical domain, whose radium is $S = 50$. An additional buffer zone lays out of the physical domain with a thickness larger than $S_{\text{BF}} = 150$. The body presents the same profile geometry as that in the experiment whilst a smaller spanwise width of $W = 1.75$ is used. Non-slip wall boundary condition is applied to part of the domain's lower boundary to approximate the stationery ground in the experiment, as well as to all body surfaces. Symmetric boundary condition is applied to the rest lower boundary and spanwise boundaries. Pressure far-field boundary condition is applied to upstream, downstream, and top boundaries to generate the freestream flow. Reynolds and Mach numbers are prescribed as $Re_H = 2.3 \times 10^4$ and $Ma = 0.2$, respectively.

The computation domain is discretized by non-structural meshes. The mesh in the boundary layers and wake

Table 1: Characteristic frequency St obtained by the experiment and DAS using variant time step sizes.

CFL	100	25	10	Exp.
St	0.2239	0.1965	0.1897	$0.182 - 0.192$

Table 2: Characteristic frequency St obtained by the experiment and DAS using variant time step sizes.

Method	δ_{99}	θ	Shape factor
Exp.	0.58	0.066	1.776
Num.	0.61	0.059	1.410

region are refined, with a surface mesh size of $y^+ = 1$, $x^+ = 20$ and $z^+ = 25.6$. The largest mesh size in the physical domain is 0.4, capable of capturing acoustic waves at frequencies up to $f = 1.25$. Meshes in the buffer zone are prescribed with large growth rates, leading to the largest size up to 40, to diminish acoustic fluctuations. In addition, the time step is prescribed as CFL = 25 based on an independence study.

3 Results and Discussion

Due to the length of this abstract, only a part of the results is presented here to compare the experimental measurements and numerical predictions. Further results will be presented in the workshop.

3.1 Validation of numerical results

Table 2 presents boundary layer properties measured at the body's upper trailing edge. It shows the DAS modelling well captures the upper boundary layer in terms of the 99%-velocity-based thickness δ_{99}, the momentum thickness θ and the character of turbulent boundary layer. Figure 3, then, presents the time-averaged velocity profiles of the near wake, illustrating the DAS modelling is capable of modelling the wake dynamics. Moreover, figure 4 presents a profile of pressure fluctuation distributed along $x = -1.82$ in plane $z = 0$ and compares it against the decay law of acoustic pressure, $p'(y) \propto y^{-0.5}$. The fluctuation amplitudes decays in according with the decay law at $y \geq 9$, while the difference at $y < 9$ possibly results from the hydrodynamic unsteadiness in the near field. Thus, the DAS resolution for solving acoustic properties is verified to be sufficient.

4 Conclusions

The flow and the induced noise of the D-shaped body in proximity to a stationery ground are investigated experimentally and numerically. Results show the flow is characterized by a leading-edge separation and reattachment over the body's upper side, massive separations from trailing edges, and a 3-D wake with intermittent vortex shedding. The acoustic far-field presents direcitvity of sound pressure in vertical and upstream directions. Significant tonal noise is captured at higher frequencies over the vortex-shedding frequency.

Due to the length of this abstract, only a part of the results is presented here. Further results will be presented in the workshop.

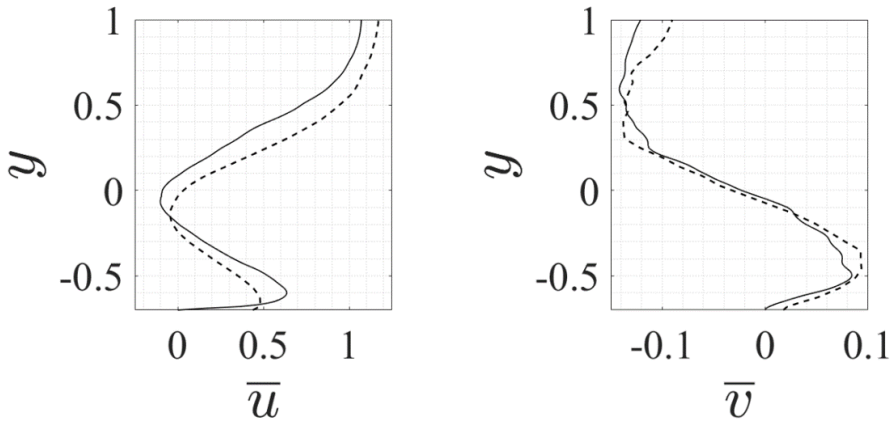

(a) Time-averaged streamwise velocity $\overline{u}$ (b) Time-averaged transverse velocity $\overline{v}$

Figure 3: Time-averaged velocity profiles of the near wake at $(x, z) = (2, 0)$: experimental (dashed lines) and numerical (straight lines) results.

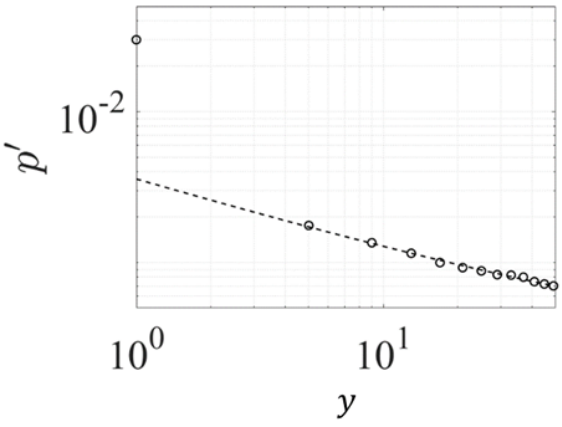

Figure 4: DAS results of pressure fluctuation distributed along $(x, z) = (-1.82, 0)$ (marked by $\circ$) and the decay law of acoustic pressure $p'(y) \propto y^{-0.5}$ (dashed line).

References

[Cowdrey, 1968] Cowdrey, C. (1968). Application of maskell's theory of wind-tunnel blockage to some large solid models. In *Proc. Symp. of Wind Effects on Buildings and Structures, Loughborough University, April*.

[Huang et al., 2021] Huang, D., Yang, Z., and Leung, R. C. K. (2021). Implementation of direct acoustic simulation using ansys fluent. In *INTER-NOISE and NOISE-CON Congress and Conference Proceedings*, volume 263, pages 1243–1252. Institute of Noise Control Engineering.

[Huang et al., 2022] Huang, G., Seid, K. H., Yang, Z., and Leung, R. C. K. (2022). Interaction and acoustics of separated flows from a d-shaped bluff body. *International Journal of Numerical Methods for Heat & Fluid Flow*, 32(4):1186–1203.

[Krajnović and Fernandes, 2011] Krajnović, S. and Fernandes, J. (2011). Numerical simulation of the flow around a simplified vehicle model with active flow control. *International Journal of Heat and Fluid Flow*, 32(1):192–200.

[Parkin et al., 2015] Parkin, D., Sheridan, J., and Thompson, M. (2015). Numerical analysis of periodic open-loop flow control on bluff bodies in ground proximity. *Journal of Wind Engineering and Industrial Aerodynamics*, 145:339–350.

[Parkin et al., 2014] Parkin, D. J., Thompson, M. C., and Sheridan, J. (2014). Numerical analysis of bluff body wakes under periodic open-loop control. *Journal of fluid mechanics*, 739:94–123.

[Pastoor et al., 2008] Pastoor, M., Henning, L., Noack, B. R., King, R., and Tadmor, G. (2008). Feedback shear layer control for bluff body drag reduction. *Journal of fluid mechanics*, 608:161–196.

Low frequency dynamics of the axisymmetric bluff body wake

Simran Singh Panesar[1]* Hao Xia[1], Martin Passmore[1]
1: Aeronautical and Automotive Engineering Department, Loughborough University, LE11 3TU, UK
* Corresponding author: s.s.panesar@lboro.ac.uk

Keywords: Wall Modelled LES, Conditional space-time POD

1 INTRODUCTION

Bluff body wake flows contain a broad range of scales which oscillate periodically with rarer events which occur stochastically. Long-time dynamics are typically associated with large turbulent structures which alter the balance of the wake region and induce non-optimal drag conditions. Similar symmetry breaking behaviours have been explored in the bi-stable wakes of rectilinear bluff bodies where is it has also been shown that across the switch between two asymmetric, reflectional symmetry breaking states an optimal symmetry preserving condition is attained [1]. With an axisymmetric wake, the instability manifests as a random reorientation of a planar shedding axis [2] with the symmetric condition offering potential base pressure drag reductions of between to 4-7% [3] which is beneficial for ground or airborne vehicles.

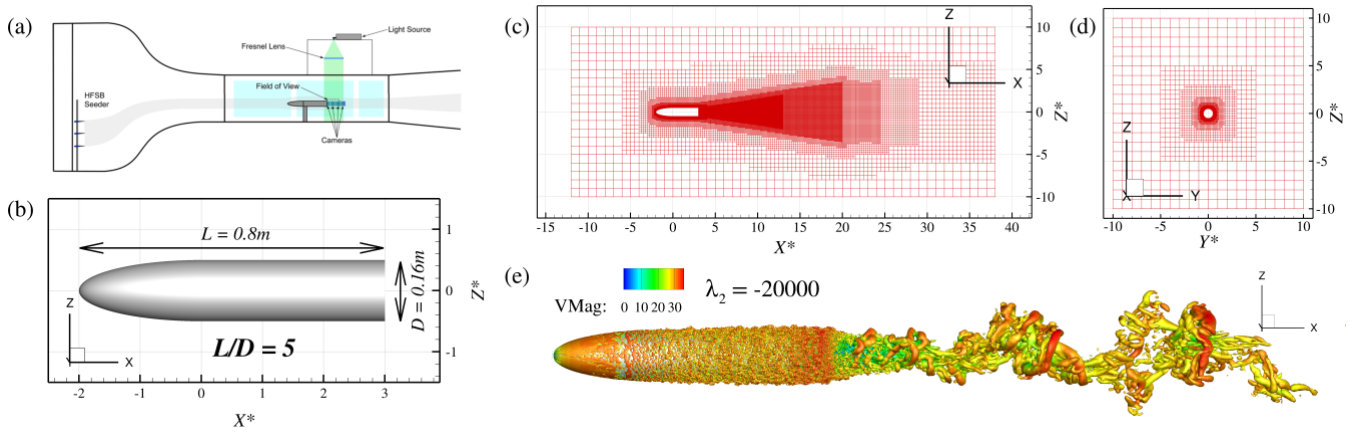

Figure 1 - Experimental and computational setup. (a) Tomographic PIV setup of Pavia et al. [3] of the axisymmetric model in (b). (c) Streamwise and (d) base-normal mesh. (e) Lambda-2 vorticity criterion for body and wake at $\lambda_2 = -20{,}000$.

In the current work, the elliptic nosed axisymmetric bluff body of Pavia et al. [3] which was studied with tomographic PIV (Fig.1(a/b)) at a Reynolds number based on diameter, $Re_D = 3.2 \times 10^5$ was studied using Wall Modelled LES. The wall shear stress is approximated using a wall function and the sub-grid scales are resolved with the WALE model. Star-CCM+ Trimmed Cell mesher was utilised to create a predominantly hexahedral grid with six prismatic layers providing a near cubic near wall mesh on the model surface and a first cell located in the logarithmic region, $y^+ \approx 60$. The total simulated time was 4650 t^* and data was sampled at 1kHz from a point cloud within the wake region up to 2D downstream of the base. Following comparisons with experimental results, the coherent structures are analysed with both azimuthal Fourier decompositions and a conditional space-time POD formulation to localise instances of flow reversal.

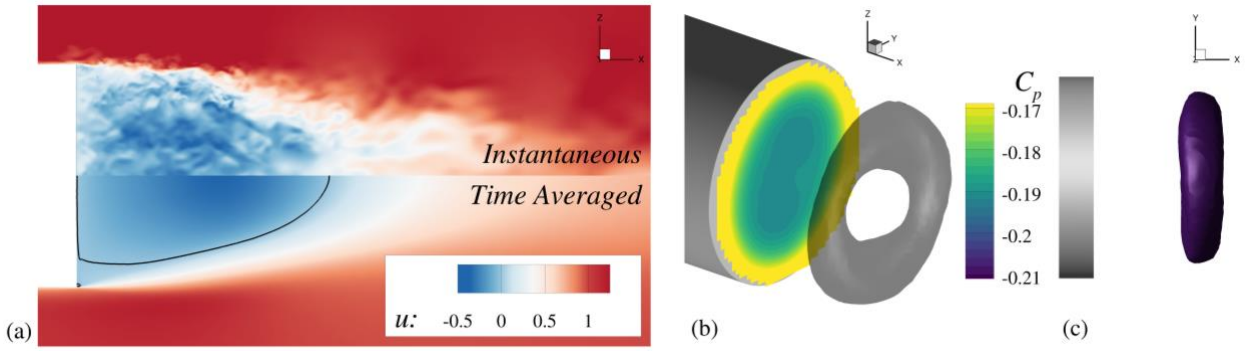

Figure 2 – (a) Time averaged results. Instantaneous (upper) and Time Averaged (lower) streamwise velocity with zero streamline showing $\bar{u} = 0$. (b) Time averaged base pressure and iso-contour of $C_p = -0.27$ in the wake.

2 RESULTS AND DISCUSSION

The time averaged recirculation length (black outline in Fig.2(a), ($L_R = 1.15$) and base pressure drag ($C_{d_b} = 0.119$) were both marginally underestimated compared with experiment. The differences are attributed to a wing support and application of a turbulence strip at $X^* = 0$ within the experiment both of which were omitted for simplicity in numerical simulations. Fig.2(b) and (c) show an iso-surface of $C_p = -0.27$ which has a near axisymmetric toroidal structure with a slight bias to the upper and lower regions of the base which is reflected in the peak suction regions showing a dipole-like distribution.

Spectral content of the polar transformed centre of pressure is shown in Fig.3(a) and (b). In agreement with studies of similar axisymmetric bluff bodies [2] showed the predominance of three frequencies, namely the vortex shedding at $St_{VS} \approx 0.2$, an axial pulsation at $St_{BP} \approx 0.08$, and an intermediate value believed to be a subharmonic of the vortex shedding with an azimuthal wavenumber of $m = 2$ at $St = 0.095$. Fig 3(c) and (d) show two-dimensional probability density functions which reveal an annular arrangement of the data consistent with that found in experiment. The white dotted line shows the average radial position which is marginally higher with WMLES than the experimental value at $r^* = 0.037$ which is likely due to the wake being pressed against the base causing larger excursions from the origin.

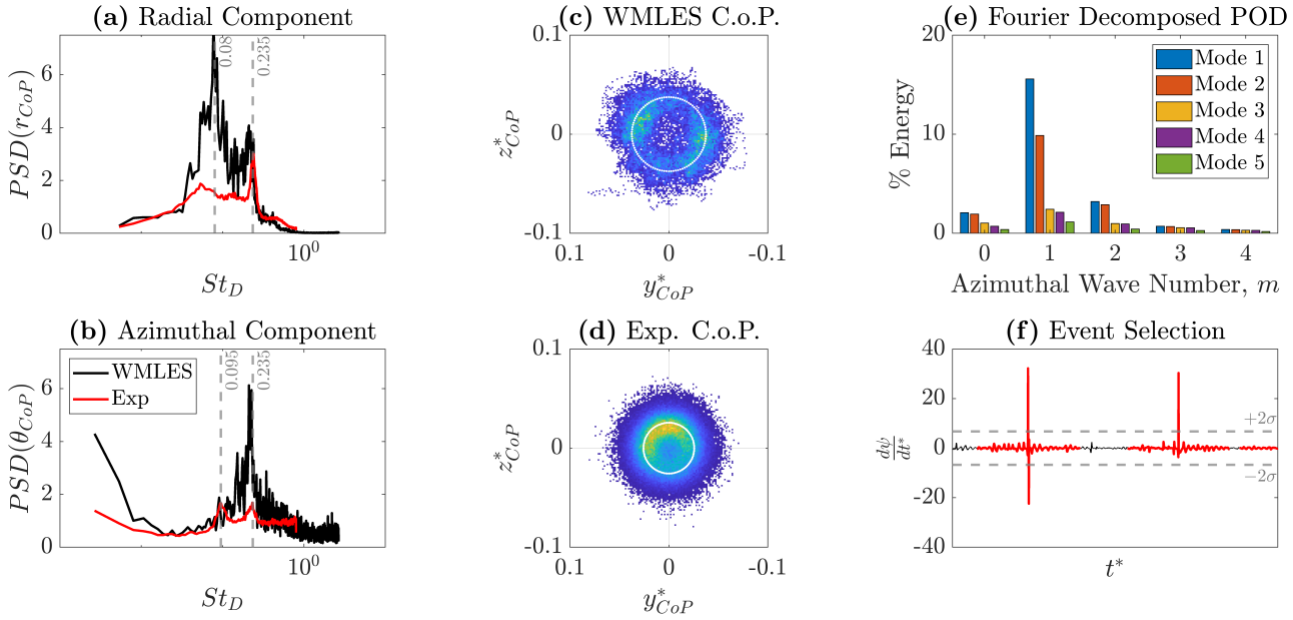

Figure 3 – Fluctuating results. Pre-multiplied spectra of the radial, r^*_{CoP}, and azimuthal, θ_{CoP}, components of the base centre of pressure (C.o.P.). Probability density functions of the corresponding data with white dotted line showing average radial position. (e) First five POD modes for the first 5 azimuthal Fourier modes of the streamwise u data. (f) Event selection sample for CST-POD with a 0.5 second window around events which exceed twice the standard deviation.

Since statistical properties of the velocity vector are axisymmetric in the azimuthal direction, a Fourier decomposition is performed for each radial row [2] of the streamwise velocity, u, up to $|m| = 43$. Subsequently, coherent structures were extracted by application of POD to assess the distribution of energy amongst the azimuthal modes. Over 15% of the fluctuating streamwise energy is contained in the first $|m| = 1$ wavenumber which is consistent with that found in the literature due to the low frequency motions also typically being anti-symmetric. The second most prominent wavenumber was $|m| = 2$ followed by the axisymmetric $m = 0$ mode.

Taking the first two spatial modes of the $|m| = 1$ wavenumber, an instantaneous angle ψ, is constructed from the temporal coefficients which resembles that of the θ_{CoP}. Unwrapping this result and performing a finite difference differentiation, the rate of change of the azimuthal component is obtained. Stochastic activity is then isolated by selection of instances which exceed twice the standard deviation in a manner similar to Stahl et al [4]. Fig.3(f) shows an example with a window size of 0.5 seconds though this will need to be refined with additional considerations for time delayed instances which can be used to smooth extracted modes. This forms the basis for the conditional space-time POD (CST-POD) which will be explored further.

3 REFERENCES

[1] Grandemange et al., Bi-stability in the turbulent wake past parallelepiped bodies with various aspect ratios and wall effects, *PoF* **25**, (2013)

[2] Pavia et al., Three-dimensional structure of the unsteady wake of an axisymmetric body, *PoF* **31** (2019)

[3] Rigas et al. Low-dimensional dynamics of a turbulent axisymmetric wake, *J. Fluid Mech.*, **778**, 1-10 (2015)

[4] Stahl et al. Conditional space-time POD extensions for stability and prediction analysis, *J. Comput. Phys*. **492** (2023)

An experimental investigation of a high Reynolds number turbulent wake generated by a vehicle-like bluff body

Samaresh Midya and Sean Symon
University of Southampton

Details about an experimental investigation of a turbulent wake (with a spanwise dimension-based Reynolds number of 3.43×10^5) generated by a vehicle-like bluff body are discussed. The mean velocities of the wake are fully characterised using stereo particle image velocimetry (PIV). Preliminary results are shown.

I. INTRODUCTION

Flow past bluff bodies is common in nature and has significant scientific and practical applications. The majority of goods transporters have bluff bodies, and the volume they must transport limits the shapes of these bodies. The boundary layer developed on bluff bodies separate easily and shed vortices. The adverse pressure gradient forces the boundary layer to separate from the body. Separation can occur either from a sharp edge or from a continuous surface. These flows produce a great deal of pressure drag in addition to skin friction drag, which raises the overall drag. As a result, the bluff bodies—including somewhat streamlined vehicle bodies—lose a lot of energy, which increases the quantity of fuel needed for motion and negatively affect the environment. Oftentimes these flows develop large scale structures thus unsteady forces which affect the stability of the body itself. Flow past bluff bodies has been the subject of several basic research. However, there aren't many experimental studies that completely charaterize each velocity component of a bluff body's turbulent wake at high Reynolds numbers. A complete charaterization of the evolution of the wake of a bluff body will shed some lights on the time and length scales of the flow structures involved. A study was conducted utilising stereo-particle image velocimetry (PIV) to fully characterise the wake of a vehicle like bluff body (as shown in figure 1) at Reynolds number 3.43×10^5 (defined as zU_∞/ν, where z is the spanwise width of the model, U_∞ is the free stream velocity, and ν is kinematic viscosity). Every velocity component was measured at cross-stream planes (i.e., $y-z$ planes) at different streamwise locations starting from the trailing edge of the model. Beginning at the trailing edge of the model, each velocity component was measured at cross-stream planes (i.e., or $y-z$ planes), at various streamwise locations. The experimental setup and measurement methods used are discussed in the following section.

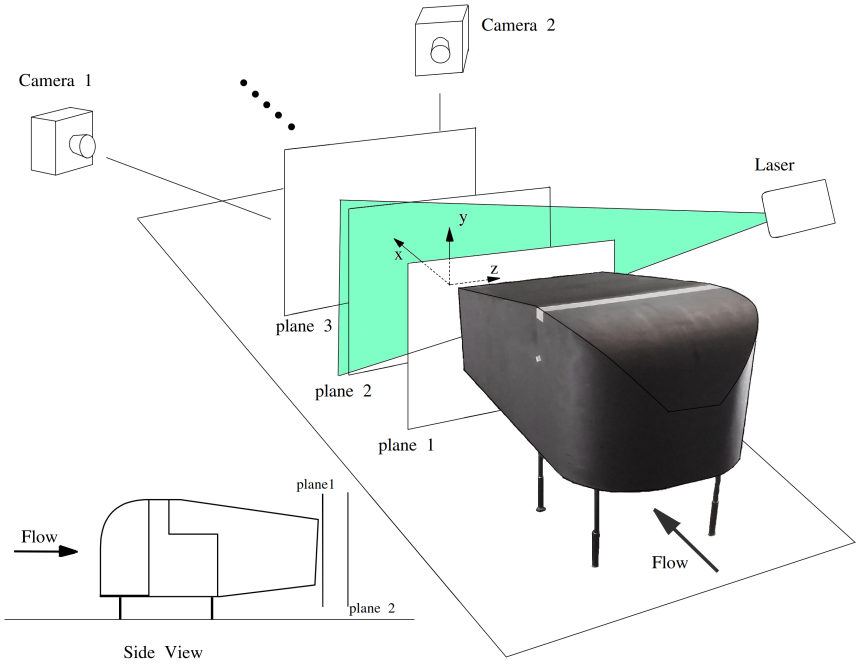

FIG. 1. Schematic of the setup. The primary directions are also shown.

II. EXPERIMENTAL FACILITIES

The experiment was conducted in the R.J. Mitchell wind tunnel facility at the University of Southampton. The tunnel is a closed-return facility of 3.6 $m \times 2.4\ m \times 10\ m$ working section with a speed range of $4 - 40\ m/s$ and a working section free-stream turbulence level of less than 0.2%. An air chiller is also included in the wind tunnel to regulate the airflow temperature. To create the wake, a free-stream velocity of 10 m/s is employed. Aluminium makes up the model's skeleton, while plywood was used to construct its surface. To minimise the laser reflection, the entire model and its supports were painted black. The model was mounted on the tunnel floor using four cylindrical columns. In order to allow the body's wake to freely evolve, the diameter of these supports was kept as tiny as feasible. The columns were connected to a cross rail whice was connected to the tunnel floor. The diameter was kept as small as possible to let the wake of the body evolve freely. A cross rail that was attached to the tunnel floor was connected to these columns. The model and the cross-rail might travel in the tunnel's streamwise direction. The wake's cross-plane was illuminated by a dual pulse laser (Litron-Bernoulli) while smoke particles were used to seed the flow. The laser plane's position was maintained constant, and the model was shifted streamwise using the aforementioned rail as needed. In this manner, velocity measurements were obtained from cross-planes at various streamwise sites. Some of the preliminary results are shown in the following section.

III. PRELIMINARY RESULTS

The wake was split into four sections because to its large cross section, and PIV was performed on each of those sections independently. To obtain the whole wake, all of the individual pieces are put together during post processing. PIVtools, an internal programme built with Python and Matlab, was used to process the data. The data was processed using in-house PIVtools, a python and matlab based code. A cross-plane sample mean streamwise velocity plot obtained at a streamwise distance of 210 mm from the trailing edge is displayed in figure 2.

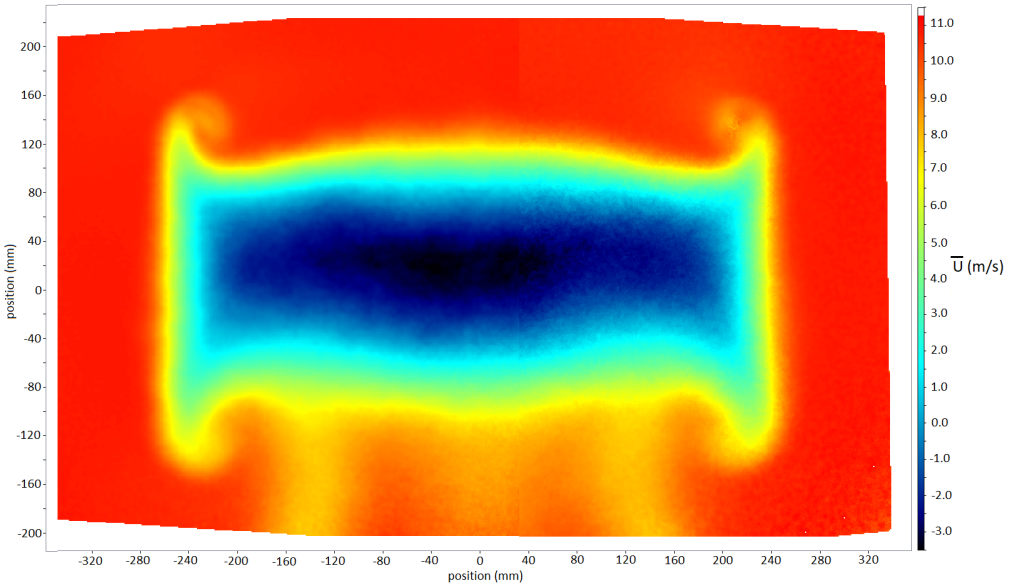

FIG. 2. Mean streamwise velocity at $x = 210\ mm$.

[1] R. Soares and K. Garry, The introduction of multiwake - an adaptable bluff-body wake emulator for ground vehicle studies, (2023).
[2] B. Podvin, S. Pellerin, Y. Fraigneau, G. Bonnavion, and O. Cadot, Low-order modelling of the wake dynamics of an ahmed body, Journal of Fluid Mechanics **927**, R6 (2021).

The near wake of the generic cyclist model

Wouter Terra[1], Andrea Sciacchitano[1,*], Siward Vloemans[2],
Christopher Brown[3], Toon Huysmans[2]
1: Dept. of Flow Physics and Technology, Delft University of Technology, The Netherlands
2: Dept. of Human-Centered Design, Delft University of Technology, The Netherlands
3: Fluids Laboratory for Aeronautical and Industrial Research (FLAIR), Monash University, Australia
* Correspondent author: a.sciacchitano@tudelft.nl

Keywords: Cycling Aerodynamics, Particle Image Velocimetry, Near Wake

1 INTRODUCTION

Cycling aerodynamics investigation focuses on aerodynamic drag reduction of the rider and bike to improve athlete's performance. Many of the studies on the topic make use of cyclist mannequins, in contrast to a real person, in a wind tunnel to ensure well-controlled and repeatable measurements (e.g. Crouch et al. 2014, Brown et al 2020, Terra et al 2020). The more recent mannequins are typically obtained by scanning individual athletes, resulting in highly realistic models (e.g. Chi et al. 2018, Terra et al 2020). The consequence of using personal anthropomorphic data, however, is that it cannot be openly shared, which makes it often difficult to compare results. To overcome this issue, in this work we introduce the Generic Cyclist Model (GCM), which reproduces the main anthropomorphic characteristics of top athletes. Because the cyclist's posture largely determines the large-scale wake flow structures and the aerodynamic drag (Crouch et al. 2014), two typical cycling postures, namely time-trial and sprint, are considered here and analyzed with a detailed characterization of the near wakes.

2 CONSTRUCTION OF THE CYCLIST MODELS

The method to construct the GCM is based on the DINED mannequin (Huysmans et al. 2020). First, fourteen endurance riders are selected to participate in this work. Each athlete was scanned in the time-trial (TT) and sprint position on their bike using *ARTEC Eva* handheld 3D scanners. The obtained scans were processed (e.g. removing parts of bike and floor) into watertight models, and a set of systematic landmarks were defined on each of them in anatomically meaningful locations. A base mesh, holding the same set of landmarks, then corresponded to each of the individual scans (Vloemans 2022) to finally average these corresponded meshes, resulting in the GCM in TT (Figure 1 top-right) and sprint position (Figure 1 bottom-right). The two digital GCMs were used to produce two physical full-scale models for wind tunnel testing. The wind tunnel models were manufactured by additive manufacturing and a primer was applied. A smooth surface was obtained through polishing with sandpaper (grain 400).

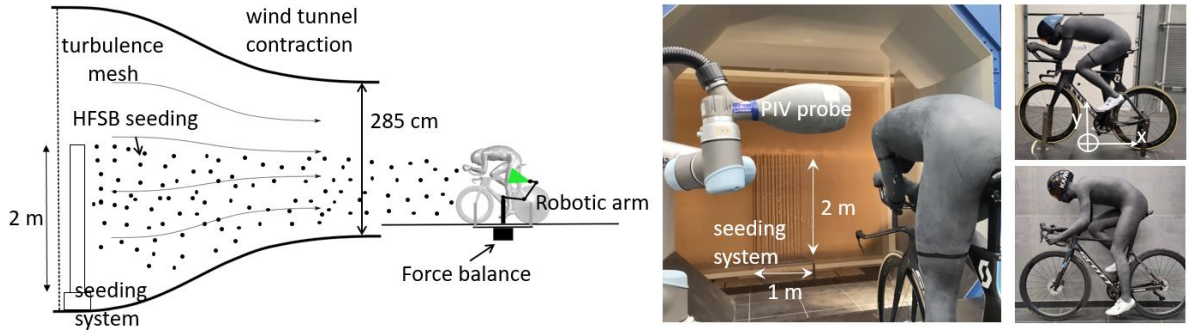

Figure 1: Schematic wind tunnel setup (left), the platform with TT model (middle) and side views of the two GCMs (right).

3 EXPERIMENTAL SETUP

The experiments were conducted in the Open Jet Facility (OJF) of the Aerodynamics Laboratories of the TU Delft. This is a closed-loop, open jet wind tunnel with an octagonal cross-section of 2.85 × 2.85 m, a linear contraction from the settling chamber to the nozzle exit of 1.7:1 and a turbulence intensity in the free-stream <0.5%. The TT model was installed on a TT bike (Scott Plasma 5 with rims brakes) wearing a Kask Minstral helmet (Figure 1-top right). The sprint GCM was installed on a road bike (Scott Addict RC with disc brakes) wearing a Kask Bambino helmet (Figure 1-bottom right). The bikes were fixed on both the front and rear axles using a supporting system connected to a force balance. The experimental setup and procedures are similar to that of Jux et al. (2018), who measured the flow all around a full-scale cyclist model using Robotic Volumetric PIV. The air was seeded using an in-house developed array of Helium-filled soap bubble generators installed in the OJF's settling chamber

(Figure 1-left and middle). The 400 generators are integrated into 15, two-meter long, vertical airfoil shaped staggered wings so that the seeded stream tube spans the entire cyclist model.
The Robotic PIV system was used to scan the flow close to and in the near wake of the model, acquiring images for 12 seconds at about 800 kHz at each probe position. The velocity information was obtained via the Shake-the-Box (Schanz et al., 2016) Lagrangian Particle Tracking algorithm, and then converted to a Cartesian grid. All measurements were conducted at a typical cycling speed of 14 m/s.

4 RESULTS

Figure 2 illustrates the near wake of the generic cyclist model in time-trial position, with an iso-surface of $u/U_\infty = 0$ and streamlines color-coded by streamwise velocity component. From the iso-surface of $u/U_\infty = 0$, it is clear that separated flow regions take place downstream of the upper arms and elbows, the stretched leg and the lower back. Conversely, no flow separation occurs downstream of the bent leg, except for the knee region. Accelerated flow regions are encountered around the shoulders, on the sides of the legs as well as in between the legs. The flow follows the curvature of the cyclist's back, producing a distinct downwash at the center of the wake, consistently with results reported in the literature (Crouch et al. 2014, Jux et al. 2018), as well as two counter-rotating vortices. The presentation at the workshop will focus on the near wake of the generic cyclist model, discussing the characteristic vortex structures and the similarities and differences between the time-trial and sprint athlete's postures.

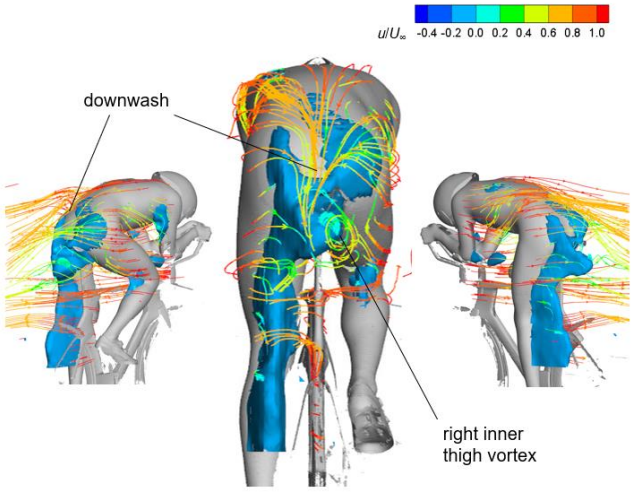

Figure 2: The near wake of the generic cyclist model in time-trial position. Iso-surface of $u/U_\infty = 0$ and streamlines color-coded by streamwise velocity component.

5 REFERENCES

Brown, C., Crouch, T., Burton, D., Thompson, M.C. (2020) Understanding the Aerodynamic Benefits of Drafting in the Wake of Cyclists. *Proceedings*, *49*, 32.

Chi, S., Pitman, J., Crouch, T., Burton, D., Thompson, M. (2021). The application of body scanning, numerical simulations and wind tunnel testing for the aerodynamic development of cyclists. *Proceedings of the Institution of Mechanical Engineers. Part P, Journal of Sports Engineering and Technology*, *235*(4), 339–353.

Crouch, T. N., Burton, D., Brown, N. A. T., Thompson, M. C., Sheridan, J. (2014). Flow topology in the wake of a cyclist and its effect on aerodynamic drag. *Journal of Fluid Mechanics*, *748*, 5–35.

Huysmans, T., Goto, L., Molenbroek, J., Goossens, R. (2020) DINED Mannequin. *Tijdschr. voor Hum Factors* 45:4-7.

Jux, C., Sciacchitano, A., Schneiders, J.F.G., Scarano, F. (2018) Robotic volumetric PIV of a full-scale cyclist. *Exp Fluids*, 59:74.

Schanz, D., Gesemann, S., & Schröder, A. (2016). Shake-The-Box: Lagrangian particle tracking at high particle image densities. Experiments in fluids, 57, 1-27.

Terra, W., Sciacchitano, A., & Scarano, F., Cyclist Reynolds number effects and drag crisis distribution, *Journal of Wind Engineering and Industrial Aerodynamics*, Volume 200, 2020.

Vloemans, S. (2022) Cyclist Mannequin For Aerodynamics Research: Develop a cyclist mannequin from 3D scans for aerodynamics tests. Master's Thesis *TU Delft Repository*.

STUDIES OF WAKE STUCTURE IN URBAN AREAS

Abhishek Mishra, Marco Placidi, Matteo Carpentieri, Alan Robins
Centre of Aerodynamics and Environmental Flow, University of Surrey, GU2 7XH, UK
Janet Barlow, Denise Hertwig
Department of Meteorology, University of Reading, UK

Mean flow, turbulence, heat transfer and pollutant dispersion within an urban canopy and in the overlying boundary layer can be disrupted by the combined wakes from a group of tall buildings (e.g. Heist et al., 2009; Brixey et al, 2009, Fuka et al., 2018; Aristodemou et al., 2018; Hertwig et al., 2019). This might well be to such an extent that makes the algorithms used in popular building wake flow and urban dispersion models inapplicable. A series of studies based largely in London, though now moving to Bristol, has sought to shed light onto these matters through the combined application of field and laboratory experimentation, and analytical and numerical modelling. Here, we concentrate on the experimental aspects based on real urban conditions. A parallel area of the work concentrates on idealised conditions, as discussed in the presentation by Mishra et al., 2023.

Our aim is to review progress through examples drawn from this work, in particular from the point of view of its practical relevance, either though developments to modelling methods used in practice, such as ADMS-URBAN and SIRANE, or the development of new models and empirical rules. The initial focus was on the small scale, individual buildings and street canyons, concentrating on the complex flows where street canyons intersect and the consequent effects on pollutant transport, as well as the transfer between the street canyon and the free flow above. This was largely the regime of the DAPPLE (2002-2010) and DIPLOS (2015-2018) projects. Here, ultra-sonic anemometry was used in the field and LDA in the laboratory to probe the flow structure. Although the focus was the processes that carried pollutant through the streets in what was broadly speaking the downwind direction, examples of significant upwind dispersion were also noted. We argued that, in these cases, the tracer that we released was captured in the recirculating flow regions behind large vehicles and then slowly detrained over a fetch that could be well in excess of 100m.

The MAGIC project (2016-2020) concentrated on the indoor-outdoor exchange of heat and pollutants, but as the field site was in the shadow of a number of tall buildings (Fig. 1), it was natural to spend some effort in addressing their impact at the experimental site. LIDAR instrumentation was now available in the field as we carried out a long duration mapping of the wakes of the tall buildings. Different approaches were used in the laboratory and field to extract the wakes from the background flow, the latter being anything but homogeneous - the assumptions used are critical for such as estimating wake decay extent.

This led to two current projects, FUTURE and ASSURE. The aims of the former include understanding the magnitude and spatial scale of the effects of a cluster of tall buildings, and their consequent impact on wind, scalar, and temperature fields, and assessing what can be said generically (i.e. modelled) and what remains site-specific. The City of London cluster was to be the field site but for a number of reasons Berlin assumed that role, though numerical and wind tunnel modelling could still address the original aims. Finally, ASSURE addresses even larger scale issues, using the city of Bristol as its exemplar. Separated flows remain of interest but in a topographical framework.

The presentation will review aspects of these projects, bringing emphasis on some of the key results and issues affecting the experimental work, and closing with discussion of some of the important question that remain.

Figure 1. Looking south from the MAGIC field site, towards the Elephant and Castle.

References

Aristodemou, E, Boganegra, LM, Mottet, L, Pavlidis, D, Constantinou A, Pain, C, Robins, A ApSimon, H. (2018). How tall buildings affect turbulent air flows and dispersion of pollution within a neighbourhood. Environmental Pollution 233, 782-796.

Brixey L, Heist DK, Richmond-Bryant J, Bowker G, Perry S, Wiener R (2009). The effect of a tall tower on flow and dispersion through a model urban neighborhood. Part 2. Pollutant dispersion. Journal of Environmental Mon- itoring 11(12):2171–2179.

Fuka V, Xie ZT, Castro IP, Hayden P, Carpentieri M, Robins AG (2018) Scalar fluxes near a tall building in an aligned array of rectangular buildings. Boundary-Layer Meteorology 167(1):53–76.

Heist DK, Brixey LA, Richmond-Bryant J, Bowker G, Perry S, Wiener R (2009) The effect of a tall tower on flow and dispersion through a model urban neighborhood. Part 1. Flow characteristics. Journal of Environmental Monitoring 11(12):2163–2170.

Hertwig D, Gough HL, Grimmond S, Barlow JF, Kent CW, Lin WE, Robins AG, Hayden P (2019). Wake characteristics of tall buildings in a realistic urban canopy. Boundary-Layer Meteorology 172(2):239–270.

Mishra, A., Placidi, M., Carpentieri, M., & Robins, A. (2023). Wake Characterization of Building Clusters Immersed in Deep Boundary Layers. *Boundary-Layer Meteorology*, *189*(1), 163-187.

Stability and dynamics of the laminar wakes of 3D prisms

E. Boujo*

In this work, we consider the laminar wakes of 3D bluff bodies with two planar symmetries, and explore the series of bifurcations they undergo as the Reynolds number increases. We combine linear stability analysis (LS), weakly nonlinear stability analysis (WNL) and nonlinear direct numerical simulations (DNS). Of particular interest are the temporal and spatial symmetries selected or broken by the bifurcations.

In a first part, we study rectangular prisms and vary systematically the body length and width (normalized by the body height) in the range $1/6 \leq L \leq 5$ and $1.2 \leq W \leq 5$, respectively, thus extending previous studies (for example Marquet and Larsson 2015[1]).

LS shows that the first bifurcation depends on the geometry (Fig. 1*a*): Hopf for large W/L and pitchfork for small W/L. In general, the leading oscillatory mode breaks the top/bottom planar symmetry, resulting in periodic vortex shedding in the vertical direction. Conversely, the leading stationary mode breaks either the top/bottom or left/right symmetry, resulting in a static wake deflection in the vertical or horizontal direction, for intermediate or small W/L, respectively.

The sequence of bifurcations at larger Re is explored in detail for $L = 5$ (Fig. 1*b*). WNL and DNS show that for $W \leq 2.25$ the flow recovers the vertical symmetry but loses the horizontal one (Fig. 2) via a supercritical ($W = 1.2$) or subcritical ($W = 2.25$) pitchfork bifurcation. This regime is reminiscent of the steady horizontal deflection observed for turbulent wakes behind wider-than-tall Ahmed bodies. Further increasing Re, the flow becomes unsteady via a Hopf bifurcation, and oscillates around either the deflected wake (small W) or the non-deflected wake (intermediate W). A new regime is observed for intermediate W and Re which, surprisingly, preserves both vertical and horizontal symmetries at all times despite the shedding of hairpin vortices from the top/bottom leading-edge shear layers. At large Re and for all W, the flow approaches a chaotic state characterized by the superposition of (i) shedding of hairpin vortices from the leading edges, and (ii) horizontal and vertical flapping of the wake.

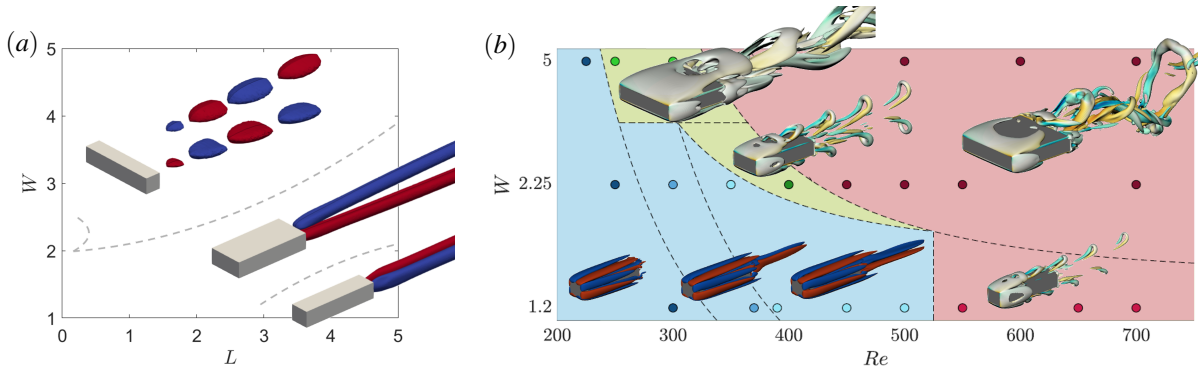

Figure 1: (*a*) Linear stability diagram: first bifurcation as a function of body length L and body width W. (*b*) Nonlinear regimes for $L = 5$, as a function of Reynolds number Re and body width W.

*École Polytechnique Fédérale de Lausanne, CH-1015 Lausanne, Switzerland

[1] Marquet and Larsson, *Eur. J. Mech. B Fluids* **49** (2015)

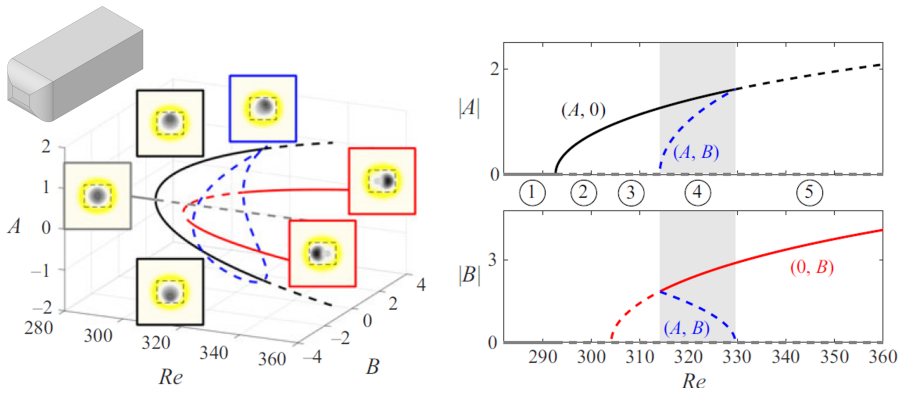

Figure 2: Weakly nonlinear bifurcation diagram from the coupled equations describing the amplitude of the vertical and horizontal symmetry-breaking modes, $\partial_t A = \lambda_A A - \chi_A A^3 - \eta_A B^2 A$ and $\partial_t B = \lambda_B B - \chi_B B^3 - \eta_B A^2 B$ (Ahmed body, $W = 1.2$, $L = 3$).

In a second part, we investigate how pitch and yaw modify the first bifurcations of an Ahmed body wake ($W = 1.2, L = 3$). As typically observed for imperfect pitchfork bifurcations, at low Re a small misalignment selects one of the steady states: vertical deflection under pitch and horizontal deflection under yaw. A small yaw angle β reduces the critical Re of the Hopf bifurcation that leads to horizontal vortex shedding. Interestingly, a small pitch angle α not only decrease the critical Re of the Hopf bifurcation that leads to vertical vortex shedding, but also increases the critical Re at which the vertically deflected state loses stability (Fig. 3*a*), resulting in a cross-over of the two bifurcations for $\alpha = 1^\circ$ (Fig. 3*b*). The flow dynamics in the vicinity of this cross-over are strongly reminiscent of the experimental observations of Grandemange *et al.* (2012)[2] for the laminar flow past an Ahmed body in ground proximity: at a constant Re, the wake first oscillates vertically before slowly transitioning to a steady horizontal deflection.

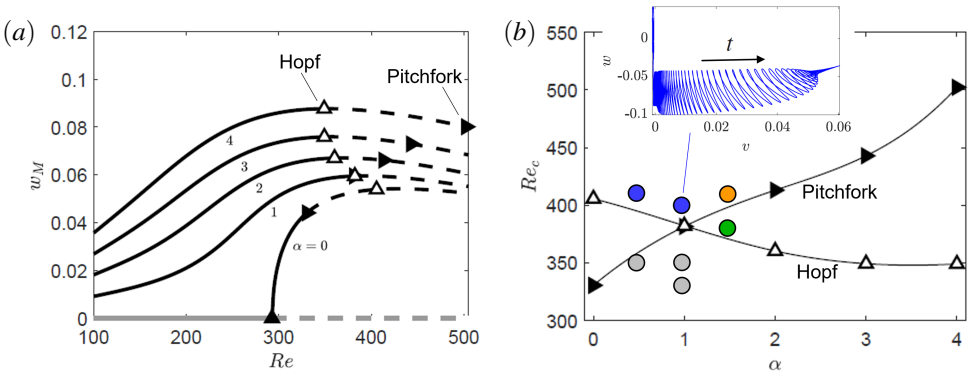

Figure 3: Effect of a small pitch angle α (Ahmed body, $W = 1.2$, $L = 3$). (a) Nonlinear base states and their linear stability. (b) Stability diagram from LS and DNS. Inset: slow dynamics from vertical vortex shedding towards steady horizontal deflection for $\alpha = 1^\circ$.

This work has been carried out in collaboration with G. Zampogna (EPFL, Switzerland) and A. Chiarini (OIST, Japan).

[2]Grandemange, Cadot and Gohlke, *Phys. Rev. E* **86** (2012)

The effect of frontal geometry on 3D bluff body wakes.

K. Janczuk[*], D. Ahmed[*], A. S. Morgans[*]

In this study we investigate numerically the dynamics of the wake past a simplified road vehicle using two canonical models; the squareback Ahmed body and the squareback Winsdor body (see Figure 1). The flow field for both cases, is simulated using Wall-Resolved Large Eddy Simulations (WRLES) at $Re_H = 3.3 \times 10^4$. Given that the primary distinction between the two bodies lies in their frontal geometry, comparing the two cases indicates the effect of fore-body modification on the wake dynamics.

The aerodynamic drag of squareback bodies, which is typical for the majority of ground vehicles, is mostly determined by the shape and dynamics of the wake. The wake forms as the airflow separates from the vehicle at its rear edges. Detached shear layers interact, giving rise to a low-energy recirculation region behind the body. This low-energy, low-pressure area is a primary contributor to the overall aerodynamic drag. Notably, both the shape and dynamics of the wake can be modified, offering the potential to reduce drag. Efficient control methods for drag reduction necessitate a comprehensive understanding of the fundamental mechanisms governing the wake dynamics. Therefore, studies focusing on the various wake topologies are essential for advancing control mechanisms aimed at drag reduction. Notably, many previous studies utilised the Ahmed body, which differs significantly from industrially relevant geometries. Investigating how findings based on the Ahmed body transfer to more intricate geometries is essential. The Windsor body serves as a valuable transitional step in this exploration. While experimental studies indicate qualitatively similar behavior in the wake of the Windsor body[1], a comprehensive numerical investigation of it is lacking. This study aims to bridge this gap by comparing the qualitative and quantitative aspects of the two wakes, thereby investigating the effect of frontal geometry on the wake. In addition to conventional methods such as comparing time-averaged flow fields, we enhance our analysis by employing 3D Spectral Proper Orthogonal Decomposition (SPOD).

The wake of a bluff body involves periodic dynamics, including vortex shedding motion, arising from Kelvin-Helmholtz instabilities in free shear layers, and a pumping motion of a ring-shaped vortex structure enclosed within the recirculation region. Additionally, the reflectional symmetry breaking that occurrs in the laminar regime and results in the wake center shifting toward one of the rear edges, persists into the turbulent region[2]. Turbulent perturbations induce the wake to switch randomly between asymmetric positions[3], leading to statistical symmetry in the wake. Notably, bi-stability contributes to 4 to 9 percent of the total pressure drag[4]. The exact mechanics governing bi-modal switching, their dependency on the geometrical features, and possible control methods are currently being investigated by various research groups. Interestingly, there is a lack of consensus in the scientific community when it comes to describing the nature of bi-modal wake structures; some groups claim a single or double horseshoe vortex[5,6], while others show a toroidal structure[7,8,9]. In addition, a recent observation noted a link between the dynamics of the upstream boundary layers along the body surfaces and wake bi-modality[8]. This motivated study suggesting that hairpin vortices generated after the front separation bubble of the Ahmed body are responsible for bi-modal switching[9]. This link provides an opportunity for new flow control strategies based on front separation bubble control. Therefore, it is of high importance to further investigate this relationship and its dependency on the geometrical features, including the very front of the geometry where the bubble is located.

SPOD results in modes oscilating at specific frequencies ranked based on the contained energy. Importantly,

[*]Imperial College London, SW7 2BX, London, England

[1]Pavia, Passmore, Varney, and Hodgson, *Journal of Fluid Mechanics* **888** (2020).
[2]Grandemange, Gohlke,and Cadot, *Journal of Fluid Mechanics* **722** (2013)
[3]Rigas, Morgans, Brackston, and Morrison, *Journal of Fluid Mechanics* **778** (2015).
[4]Grandemange, Gohlke, and Cadot, *Journal of Fluid Mechanics* **752** (2014).
[5]Evrard, Cadot, Herbert, Ricot, Vigneron, and Délery, *Journal of Fluids and Structures* **61** (2016).
[6]Perry, Passmore, and Sardu, *Experiments in Fluids* **59** (2017).
[7]Dalla Longa, Evstafyeva, and Morgans, *Journal of Fluid Mechanics* **866** (2019).
[8]Hesse, and Morgans, *Computers & Fluids* **223** (2021)
[9]Ahmed, and Morgans, *Journal of Fluid Mechanics* **975** (2023)

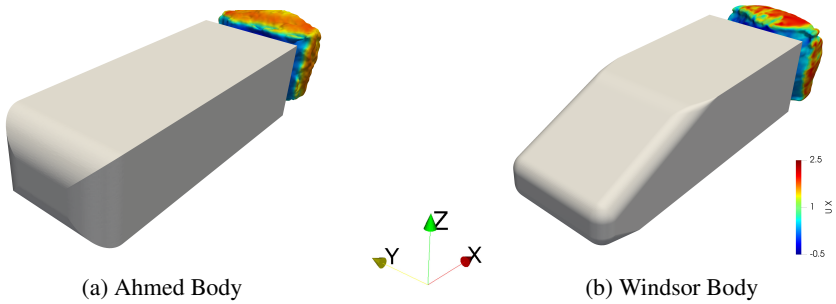

(a) Ahmed Body (b) Windsor Body

Figure 1: Visual representation of geometries and the toroidal-vortex structures in the near-wake regions, defined as iso-surface of $Cp = -0.22$ coloured by the time-averaged streamwise velocity.

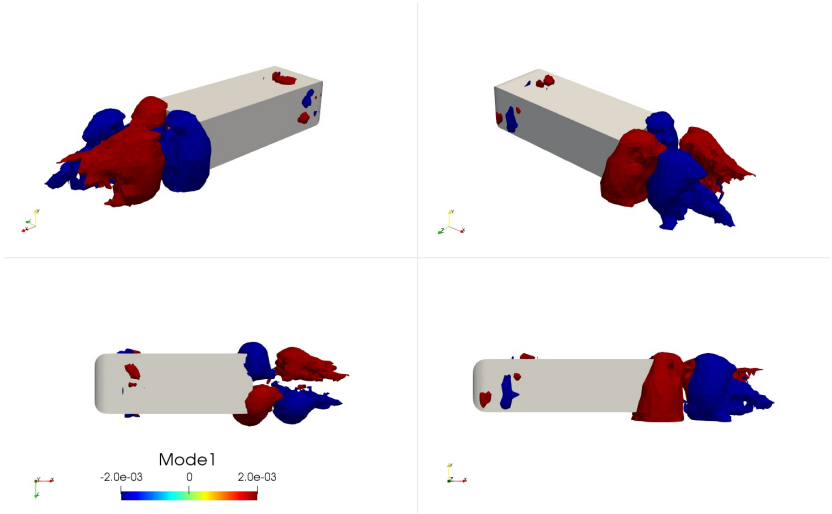

Figure 2: 3D SPOD results of the Ahmed body: iso-volumes of mode-1 at StW = 0.006, associated with wake horizontal bi-modality. The top row shows a three-dimensional view of the wake on both sides of the body. The bottom row shows a top-view of the domain (left) and a side view of the body (right).

the modes are orthogonal and optimal which provides an advantage over classical Dynamic Mode Decomposition or Proper Orthogonal Decomposition (POD). The fundamental concept behind SPOD involves partitioning the data realisations into distinct blocks, with the potential for overlaps between these blocks. Subsequently, the data undergoes Fourier transformation into the frequency domain and is then rearranged based on frequency. At each frequency, POD is applied, generating optimal orthogonal modes that oscillate at the corresponding frequency. SPOD modes capture structures that exhibit coherent evolution in both space and time, distinguishing them from spatial-only POD modes, which typically lack such coherence. While prior numerical studies applied 2D SPOD to ground vehicles[10], the introduction of 3D SPOD in this study represents a novelty. The extraction of 3D coherent structures offers a deeper understanding of flow behavior and contributes significantly to advancing our insights into the intricacies of the phenomenon.

A 3D SPOD analysis of the wake of the Ahmed body shows that the three-dimensional views of the wake structures linked to various SPOD modes serve as an effective tool for investigating the dynamics of the wake. The investigation not only shows the presence of three distinct dynamical modes in the wake: stochastic bi-modal switching, periodic bubble pumping, and vortex shedding in both cross-flow directions, but also facilitates linking the dynamics related to boundary layer separation at the front of the body with bi-modal switching, as depicted in Figure 2. Preliminary results from the Windsor body simulation exhibit qualitatively similar findings, depicted in Figure 1. However, a quantitative comparison awaits the accumulation of sufficient data necessary for conducting 3D SPOD analysis.

[10] Schmidt, Woszidlo, Nayeri, and Paschereit, *Experiments in Fluids* **59** (2018).

Random switching dynamics and low frequency oscillations around airfoil stall

Ivan Kharsansky Atallah[*], Luc Pastur[*], Romain Monchaux[*] and Laurent Zimmer [†]

We study experimentally the stall over a thin symmetric airfoil (NACA0012) by means of a synchronized PIV-force and pressure measurements. We have found a critical Reynolds number from which the flow transitions from a classical low-frequency oscillations regime [1] [2] to random bistable dynamics. In this regime, the flow switches randomly between a high lift state and a low lift state with residence times orders of magnitude larger than any timescale of the flow. We conditioned the PIV fields of both regimes using the lift coefficient signal. For the bistable case, the signal was binarized taking everything above the mean as part of the high lift state and everything below the low lift state. The lift-conditioned PIV fields (Fig.1 &2) confirm that the high lift state corresponds to a mostly attached flow and the low lift state to a massive separation of the boundary layer. A similar approach was followed for the low frequency regime. The phase averaged flow fields associated with the low frequency oscillations exhibit a cyclic phenomenon located in the upstream bubble of recirculation (see Fig.3). Using the time series of force and pressure measurements, we conducted a statistical analysis on the random dynamics, revealing a memoryless process with extreme events. Making use of extreme value theory, we propose a method to determine the bifurcation points of the system in an unambiguous manner, without the need to define arbitrary thresholds [3]

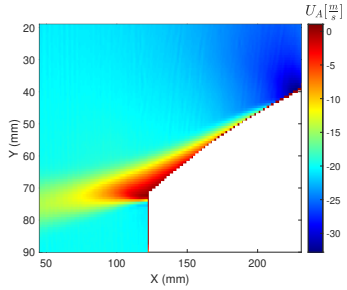

Figure 1: Mean Streamwise velocity attached state in the bistable regime.

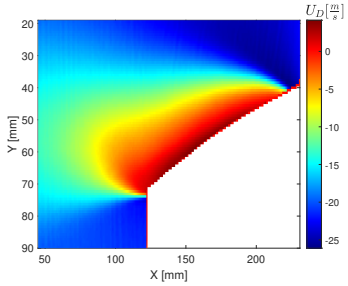

Figure 2: Mean Streamwise velocity detached state in the bistable regime.

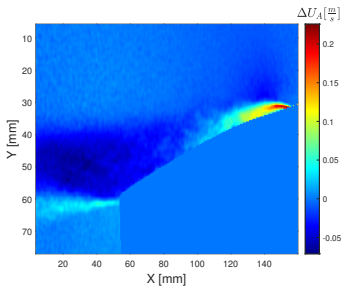

Figure 3: Mean Streamwise velocity attached phase in the low frequency regime

[*]LMI-UME, ENSTA-Paris, Institut Polytechnique de Paris, F-91120 Palaiseau, France
[†]EM2C Laboratory, CNRS, CentralSupelec, Université Paris-Saclay, 8-10 rue Joliot-Curie, 91190 Gif-sur-Yvette, France
[1]Zaman et al., J. Fluid Mech. **202**, 403 (1989).
[2]Busquet et al., J. Fluid Mech. **928**, A3 (2021).
[3]Faranda et al., New Journal of Physics. **16**, 8 (2014).

Stochastic modelling of the wake reversal dynamics of a bluff body under different Reynolds numbers

Yajun Fan*, Olivier Cadot† and Edouard Boujo‡

The turbulent wake behind a three-dimensional bluff body (Fig. 1a) manifests stochastic reversals between two asymmetric states, referred to as P and N states. Fig. 1(b) presents their velocity field in a streamwise cross-section ($x/H = 0.5$). A simple way to monitor the wake state is to compute the base pressure vertical gradient g_z through four pressure taps (blue dots in Fig. 1a). As shown in Fig. 1(c), the wake reversal dynamics is captured by the random switching of g_z between the positive value of the P state and the negative value of the N state. The dimensionless switching rate N_0^* (number of switching events per dimensionless time) is found to decrease when the Reynolds number Re_H increases[1] within the range of 10^4 to 10^5. Stochastic modelling is investigated to recover the effect of Re_H on the natural switching dynamics. Here, a first-order stochastic differential equation (Langevin equation) is used to model the wake dynamics,

$$\frac{dg_z}{dt} = -a - bg_z - cg_z^2 - dg_z^3 + \sqrt{2\Gamma}\xi(t), \tag{1}$$

with $\xi(t)$ an additive white noise, and the parameters are identified[2,3] from experimental time series of $g_z(t)$. Simulated signals $g_z(t)$ obtained by solving Eq. (1) have statistical and dynamical features similar to the experimental ones (Fig. 1c). As shown in Fig 1(d), the trend of the experimental switching rate (black) is well captured by the identified stochastic model, both with Monte-Carlo simulations (red) and with the theoretical Eyring-Kramers prediction in the low-noise limit (blue). Further investigation will focus on the mechanism by analysing the model parameters.

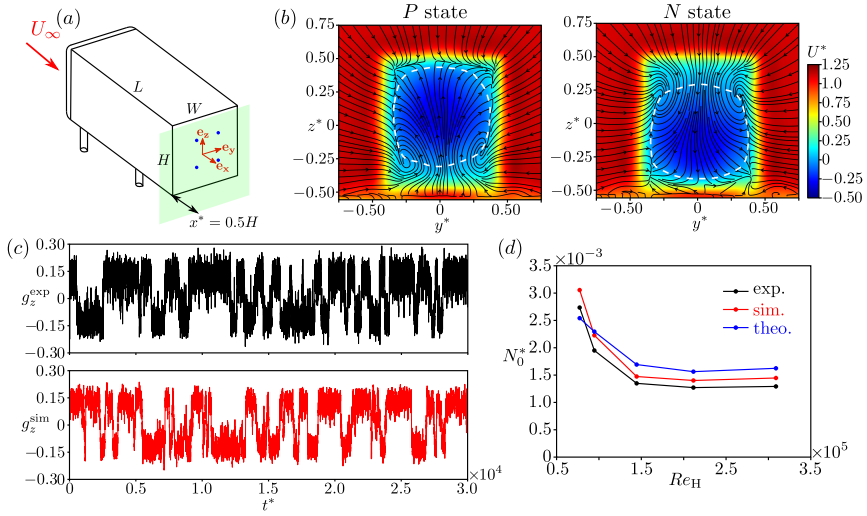

Figure 1: (a) experimental setup; (b) velocity field of two wake states; (c) time series of the base vertical pressure gradient g_z (top: experimental; bottom: simulated with the identified model); (d) variation of the switching rate N_0^* with Re_H (experiments, Monte-Carlo simulations, and low-noise Eyring-Kramers prediction).

*University of Liverpool, Liverpool L69 BX7, United Kingdom
†University of Liverpool, Liverpool L69 BX7, United Kingdom
‡École Polytechnique Fédérale de Lausanne, CH-1015 Lausanne, Switzerland

[1]Fan and Cadot, *Phys. Rev. E* **107** (2023)
[2]Böttcher et al., *Phys. Rev. Lett.* **97** (2006)
[3]Boujo and Noiray, *Proc. R. Soc. A* **473** (2017)

Influence of porous material on the flow behind backward-facing step - experimental study

L. Klotz[1], K. Bukowski[1], and K. Gumowski[1]

[1] Warsaw University of Technology, Faculty of Power and Aeronautical Engineering, ul. Nowowiejska 24, 00-665 Warszawa, Poland

E-mail: lukasz.klotz@pw.edu.pl

Abstract.

We investigate effect of porous insert located upstream of the separation edge of backward-facing step (BFS) in early transitional regime as a function of Reynolds number. This is an example of hydrodynamic system that is a combination of separated shear flow with large amplification potential and porous materials known for efficient flow destabilisation. Spectral analysis reveals that dynamics of backward facing step is dominated by spectral modes that remain globally coherent along the streamwise direction. We detect two branches of characteristic frequencies in the flow and with Hilbert transform we characterise their spatial support. For low Reynolds numbers, the dynamics of the flow is dominated by lower frequency, whereas for high enough Reynolds numbers cross-over to higher frequencies is observed. Increasing permeability of the porous insert results in decrease in Reynolds number value, at which frequency cross-over occurs. By comparing normalized frequencies on each branch with local stability analysis, we attribute Kelvin-Helmholtz and Tollmien-Schlichting instabilities to upper and lower frequency branches, respectively. Finally, our results show that porous inserts enhance Kelvin-Helmholtz instability and promote transition to oscillator-type dynamics. Specifically, we observe that amplitude of vortical (BFS) structures associated with higher frequency branch follows Landau model prediction for all investigated porous inserts.

Keywords: Experimental Fluid Mechanics, Hydrodynamics, Backward-Facing Step, Porous Materials, Vortical Coherent Structures

1. Experimental measurements of the flow behind a backward-facing step (BFS)

We investigate vortical BFS structures that are generated behind the sudden expansion of the geometry, i.e. backward-facing step (BFS) as shown in Fig. 1. We measure the velocity with Particle Image Velocimetry to quantitatively characterise these structures. An example of the spatial distribution of the measured wall-normal velocity component is shown in Fig. 1 as an alternating street of positive (in red) and negative (in blue) velocity fluctuations. We characterise these BFS structures using spectral analysis in analogy to the methodology described elsewhere [1]. Specifically, we observe a narrow-band spectrum with a characteristic frequency that corresponds to shedded vortices. In addition, we determine the dependence of the characteristic frequency and their amplitude on the Reynolds number. Our analysis is concentrated on the first instabilities of the laminar flow that occur at low Reynolds numbers.

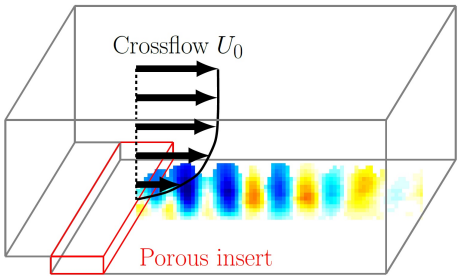

Figure 1. Geometrical configuration of backward-facing step under investigation. Black profile represents the shear flow directly upstream of the boundary layer separation at the top step corner characterised by free stream velocity U_0. Red volume represents the location, at which the replaceable porous insert is placed. Blue and red contours illustrate the spatial distribution of wall-normal velocity component that represents the BFS structures formed downstream of the separation edge.

2. Quantitative characterisation of the flow structures formed downstream of a separation edge

We estimate the critical Reynolds number, above which the BFS coherent structures emerge. Spectral analysis reveals that the dynamics of backward facing step is dominated by spectral modes that remain globally coherent along the streamwise direction. We detect two branches of characteristic frequencies in the flow and with Hilbert transform we characterise their spatial support. By comparing normalized frequencies on each branch with local stability analysis, we attribute physical mechanisms for both observed frequencies. Finally, our results show that porous inserts enhance the amplitude of one of the characteristic branches and promote transition to oscillator-type dynamics.

3. Effect of porous material on the flow structures formed downstream the separation edge

Another parameter under consideration in our study is the permeability of porous inserts located directly upstream of the separation edge. We consider three different inserts along with a reference case with impermeable walls. Using a second independent experimental installation we characterise the permeability of each of three porous inserts under investigation. The effect of porous medium on coherent BFS structures is evaluated, which includes the determination of characteristic frequency and amplitude of shedded vortices. We observe that the permeability of the fluid-solid interface can be an effective method for passive control of the flow behind a backward-facing step.

Acknowledgments

This research was funded in fraction by National Science Center (Poland) within OPUS-21 project (2021/41/B/ST8/03142).

References

[1] *"Experiments on a jet in a crossflow in the low-velocity-ratio regime"*, L. Klotz, K. Gumowski and J.E. Wesfreid, Journal of Fluid Mechanics, 2019, pp. 386-406, vol. 863

[2] *"Influence of porous material on the flow behind backward-facing step - experimental study"*, L. Klotz, K. Bukowski and K. Gumowski, under consideration for publication in Journal of Fluid Mechanics

SELF-ADAPTIVE FLAPS FOR DRAG REDUCTION IN THE AHMED BODY WAKE

M. Lorite-Díez*[1,2]
[1] *Instituto Interuniversitario de Investigación del Sistema Tierra en Andalucía (IISTA). Universidades de Granada, Jaén and Córdoba, Spain.*
[2] *Departamento de Mecánica de Estructuras e Ingeniería Hidráulica. Universidad de Granada, Granada, Spain.*
Contact: mldiez@ugr.es.

Heavy vehicles, such as trucks and buses, are a major contributor to global greenhouse gas emissions. Typically, these vehicles have blunt geometries, which are in part responsible for their poor aerodynamic performance, due to the massive flow separation at the vehicle's rear edges. As a result, a low-pressure zone, known as recirculation bubble, is created, leading to high aerodynamic drag force. Academic studies usually employ simplified models of road vehicles, as the square-back Ahmed body, which exhibits various unsteady phenomena that are representative of real vehicle aerodynamics, including vortex shedding, recirculation bubble pumping, and the reflectional symmetric breaking (RSB) mode. This latter mode can induce quasi-static switching between asymmetric wake deflected states [1], generating side forces that impact drag [2].

To control the wake behind these models, various rear passive drag reduction systems, based on base pressure recovery, have been studied in the literature [3]. For instance, the implementation of rear cavities and flaps has led to a significant reduction of the drag coefficient, however, their performance under yawed conditions, common in real conditions, decreases [4]. Therefore, the use of self-adaptive systems may constitute an appealing approach, as the flaps can passively reconfigure to different flow orientations.

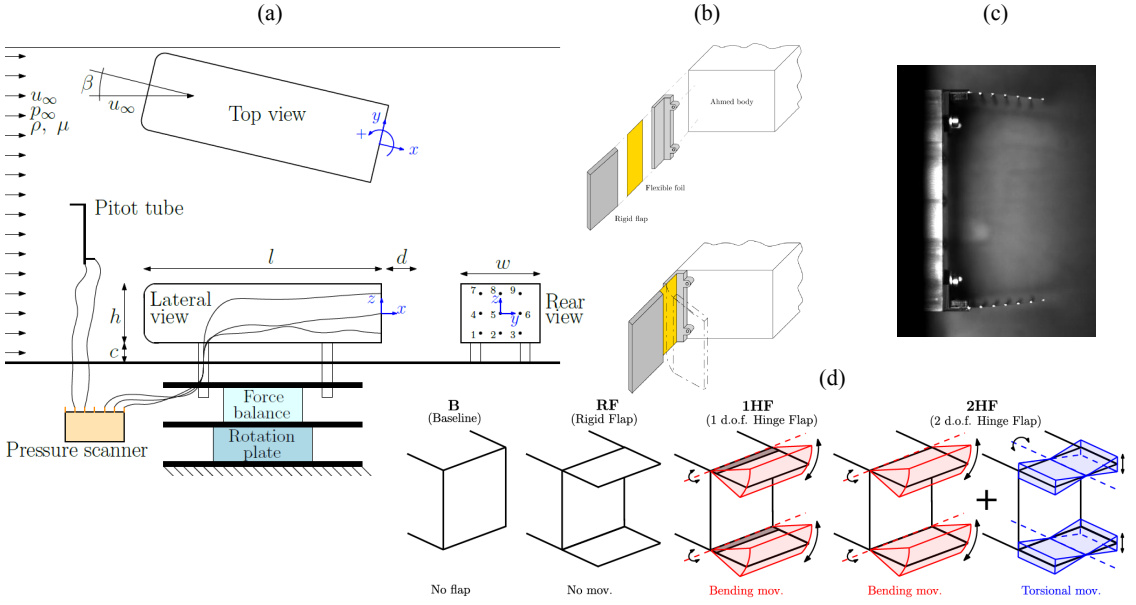

Figure 1: (a) Sketch of the experimental set-up. (b) Detail of the flexibly-hinged flap system. (c) Illustration of the instantaneous deflection of the flexible flaps at $Re \simeq 7.7 \cdot 10^4$. (d) Rear passive devices with different degrees of freedom.

Our ongoing research use the experimental set-up depicted in Fig. 1(a). There, we have tested different devices: 1 degree-of-freedom flexibly-hinged flaps [5], 2D flexible flaps and 2 degrees-of-freedom flexibly-hinged flaps, see respectively Fig. 1(b, c, d). These devices are employed to evaluate their response and the corresponding aerodynamic performance under different flow conditions: varying incoming wind velocities and the relative orientation, β, between the model axis and the incoming freestream. Usually, force, pressure, deformation and velocity measurements have been performed to characterize the response of the flaps and their effect in the near wake behind the Ahmed body.

The results show that the proposed adaptive devices are able to decrease the drag over a certain range

of flexibility, in a more efficient way that equivalent rigid flaps. These flaps undergo a passive reconfiguration in the inward direction, decreasing the bluffness of the flow separation occurring at the body base what induces the reduction of the size of the recirculation region, thus increasing the base pressure and increasing the drag. The aerodynamic improvement given by self-adaptation of flaps is even greater under yawed conditions.

These adaptive flaps are also shown to interact with the Reflectional-Symmetry-Breaking (RSB) mode, typically present in the wake of three-dimensional bodies. In that regard, the self-adaptive flaps deflect following changes in the horizontal base pressure gradient, g_y, given by the switches between states of the RSB mode, thus describing a bi-stable behaviour (see Fig. 2). The interaction of the RSB mode and the adaptive flap deflection offers new perspectives on this fundamental question which requires further experimental investigations.

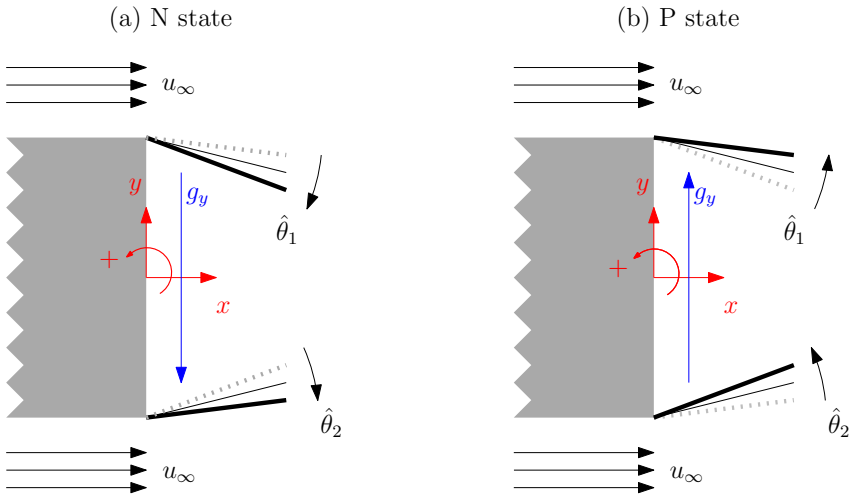

Figure 2: Sketch of the interaction between flaps and the RSB mode (a) N state observed with negative flaps deflection and (b) P state observed with positive flaps deflection. Flaps are represented using thick solid lines, while thin solid lines indicates mean deflected positions. Dashed lines are the flaps deflection of the opposite state that is not observed.

*This research is being developed with J.I. Jiménez-González, C. García-Baena, J.M. Camacho-Sánchez, J.C. Muñoz-Hervás and C. Martínez-Bazán. This work is a result of the Projects TED2021-131805B-C21 and TED2021-131805B-C22, financed by the Spanish MCIN/AEI/10.13039/501100011033/ and the European Union NextGenerationEU/PRTR.

References

[1] M. Grandemange, M. Gohlke, and O. Cadot. Turbulent wake past a three-dimensional blunt body. Part 1: Global modes and bi-stability. *J. Fluid Mech.*, 722:51–84, 2013.

[2] G. Bonnavion and O. Cadot. Unstable wake dynamics of rectangular flat-backed bluff bodies with inclination and ground proximity. *J. Fluid Mech.*, 854:196–232, 2018.

[3] H. Choi, J. Lee, and H. Park. Aerodynamics of heavy vehicles. *Annu. Rev. Fluid Mech.*, 46 (1):441–468, 2014.

[4] M. Lorite-Díez, J. I. Jiménez-González, L. Pastur, O. Cadot, and C. Martínez-Bazán. Drag reduction on a three-dimensional blunt body with different rear cavities under cross-wind conditions. *J. Wind Eng. Ind. Aerod.*, 200:104145, 2020a.

[5] J. M. Camacho-Sánchez, M. Lorite-Díez, J. I. Jiménez-González, O. Cadot, and C. Martínez-Bazán. Experimental study on the effect of adaptive flaps on the aerodynamics of an ahmed body. *Phys. Rev. Fluids*, 8(4):044605, 2023.

Examination of mass flux equilibrium in the 3D turbulent wake of the flat-back Ahmed body using stacked stereoscopic PIV

T.I. Khan[1], L. Pastur[2], O. Cadot[3] and V. Parezanović[1]

[1] Khalifa University of Science and Technology, Abu Dhabi, UAE
[2] ENSTA-ParisTech, Paris, France
[3] University of Liverpool, Liverpool L69 3GH, UK

Turbulent wake of a 3D square-back Ahmed body exhibits a long-time bi-stable behavior, referred as the Reflectional Symmetry Breaking (RSB) mode [1]. The transient asymmetric wake state is associated to a higher base drag, hence different strategies are being explored to achieve effective control over the RSB mode. More recently, we presented the effect of steady jet actuation from the center of the base [2]. The method proved to be efficient in terms of completely symmetrizing the wake along with greater drag reduction, as opposed to base blowing being carried out near the peripheral edges of the base [3].

In the present study, the three-dimensional nature of the Ahmed body wake subject to centralized base blowing is investigated. The instantaneous 2D-3C velocity fields in 30 cross-stream yz-planes in the near wake are captured using a stereoscopic particle image velocimetry (SPIV) technique, as shown in Fig 1(a). The statistically-converged SPIV fields are interpolated to obtain the time-averaged 3D wake field. Synchronous acquisition of PIV laser trigger signal along with time-resolved base pressure gradient information for each downstream plane is used to obtain conditionally-averaged vector fields. Fig 1(b) shows the symmetrizing effect of the optimal base blowing case in the mid-horizontal plane.

A flux analysis is carried out for the first time for a 3D turbulent wake, inspired by the model proposed by Gerrard [4]. The simple model for 2D wakes proposes the formation length to be linked to the balance of fluxes feeding and emptying the recirculation region. The notion of flux balance in the wake has only recently been put to test in the experiments for a mean recirculating flow aft of a ramp by Stella et al. [5]. They demonstrate a net zero balance accounting for the fluxes entering and leaving through the recirculation region interface. Using the same approach, we extend this analysis to the 3D wake by accounting for fluxes across the recirculation bubble (iso-surface of $u^* = 0$). Fig 2(a) shows the distribution of normal velocity on this surface where the influx region (identified by negative V_n^*) presents an analogy to the induced backflow into the recirculation region. Another aspect of the flux balance is the outflow by means of entrainment along the length of the shear layers. The entrainment flux is estimated by accounting for growth rate along the shear layer interface (defined by iso-surface of $u^* = 0.5$, as shown in Fig 2(b)). By performing the flux budget analysis for the natural wake and for select actuation flow rates (additional influx into the recirculation region), we identify the drag reduction mechanism through two regimes; the *mass regime* and the *favorable momentum regime*. The former is identified through an affine relationship between drag reduction and base blowing, whereas the latter is observed to introduce non-linearities by affecting the flux feeding the recirculation region. The transition between the two regimes is identified through the increased drag reduction potential as well as pronounced effect on wake asymmetry suppression. The effect on the coherent wake structures is examined using Proper Orthogonal Decomposition of the 3D velocity field.

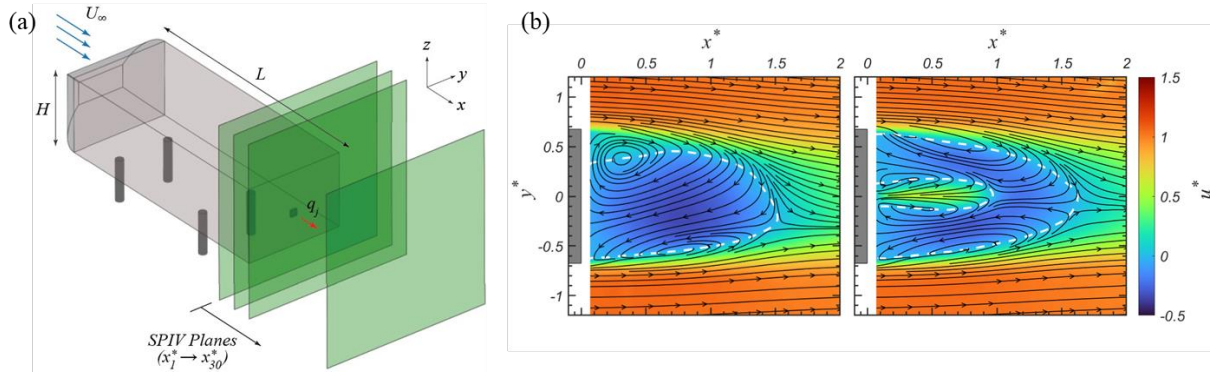

Fig 1. (a) Schematic of few traversing SPIV laser planes which constitute a swept volume for constructing three-dimensional velocity field. Flow actuation is carried out through centralized steady jet base blowing (q_j). (b) Mean streamwise velocity distribution overlaid with streamlines at horizontal plane for the natural *N*-state wake and optimally actuated symmetrized wake. The white dashed line shows the recirculation bubble as iso-line of $u^* = 0$.

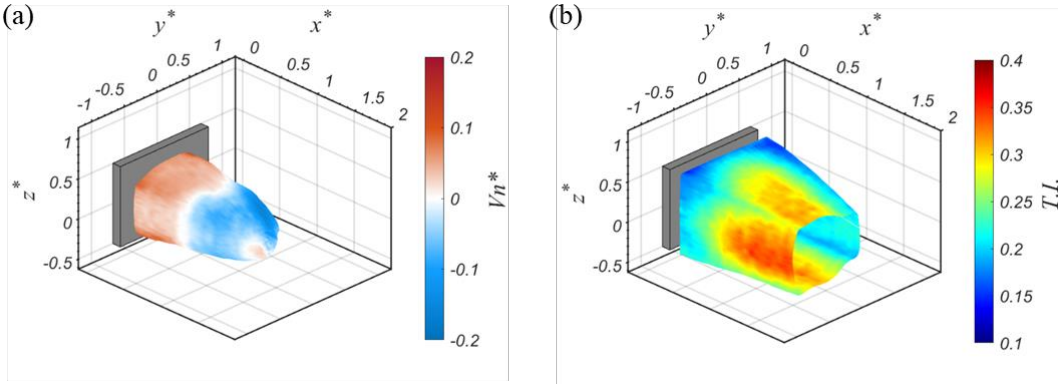

Fig 2. Characteristic surfaces for the conditionally-averaged natural wake. (a) Normal velocity (V_n^*) distribution that contribute to fluxes across the recirculation region interface (defined by iso-surface of $u^* = 0$). (b) Distribution of turbulence intensity within the shear layers characterized on the shear layer interface (defined by iso-surface of $u^* = 0.5$).

Acknowledgements

This research has been supported by the Khalifa University of Science and Technology under Award No. CIRA-2019-025.

References

[1] Grandemange, Mathieu, Olivier Cadot, and Marc Gohlke. "Reflectional symmetry breaking of the separated flow over three-dimensional bluff bodies." *Physical review E* 86.3 (2012): 035302.
[2] Khan, T. I., Parezanović, V., Pastur, L., & Cadot, O. (2022). Suppression of the wake steady asymmetry of an Ahmed body by central base bleed. Physical Review Fluids, 7(8), 083902.
[3] Lorite-Díez, M., et al. "Experimental analysis of the effect of local base blowing on three-dimensional wake modes." Journal of Fluid Mechanics 883 (2020).
[4] Gerrard, J. H. (1966). The mechanics of the formation region of vortices behind bluff bodies. Journal of fluid mechanics, 25(2), 401-413.
[5] Stella, F., Mazellier, N., Joseph, P., & Kourta, A. (2018). Mass entrainment-based model for separating flows. Physical Review Fluids, 3(11), 114702.

ON THE ROLE OF BLOWING CONFIGURATION FOR EFFICIENT DRAG REDUCTION OF A 3D BLUNT BODY

J. M. Camacho-Sánchez[1,2], M. Lorite-Díez[2,3], J.I. Jiménez-González[1,2], C. Martínez-Bazán[2,3]
[1] *Dpto. de Ingeniería Mecánica y Minera. Universidad de Jaén, Jaén, Spain.*
[2] *Instituto Interuniversitario de Investigación del Sistema Tierra en Andalucía (IISTA). Universidades de Granada, Jaén and Córdoba, Spain.*
[3] *Dpto. de Mecánica de Estructuras e Ingeniería Hidráulica. Universidad de Granada, Granada, Spain.*
Contact: jmcamach@ujaen.es.

Heavy vehicles are a major source of CO_2 emissions resulting from a large fuel consumption that is mostly due to a poor aerodynamic performance and, particularly linked to the bluff geometry. The flow around trucks and buses separates at their rear edges, creating a large recirculation bubble that creates low pressure at the base and an associated high drag coefficient. Several efficient strategies have been proposed to reduce the drag of this type of vehicles in the literature [1], including the base blowing or base bleed. This control strategy is able to recover the base pressure by injecting fluid in the base of the blunt-based body, what modifies the near wake and enlarges the recirculation region, as shown in [2]. The present study aims to bring new knowledge about how the blowing configuration may affect the drag and wake manipulation. Thus, we compare the performance of various symmetric base blowing configurations, carrying out wind tunnel experiments to analyze the impact of the blowing geometry on the aerodynamic forces, the base pressure recovery, and the near wake dynamics.

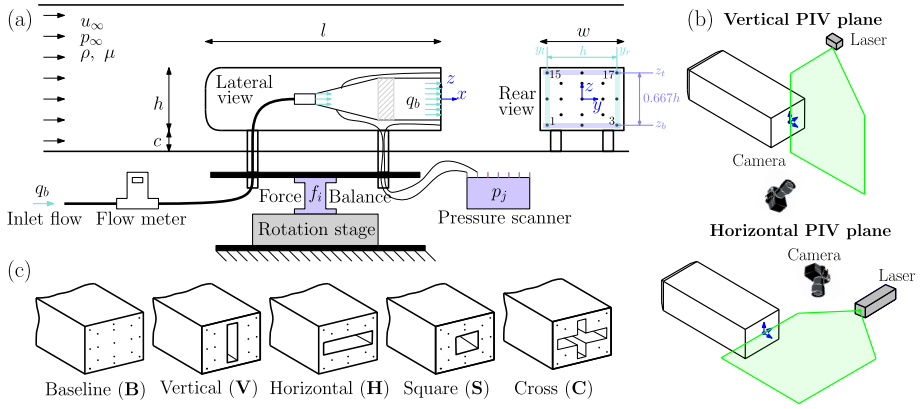

Figure 1: Sketch of the performed experiments. (a) Lateral and rear view of the Ahmed body inside the wind tunnel. (b) Planar PIV arrangements in vertical and horizontal planes. (c) Studied configurations.

We experimentally studied the flow around an square-back Ahmed body, depicted in Fig. 1, of height $h = 72$ mm, width $w = 97.25$ mm and length $l = 261$ mm in a recirculating wind tunnel. The clearance from the wind tunnel ground and the yaw angle were set at $c = 20$ mm and $\beta = 0°$ respectively. The incoming flow was defined by its velocity, $u_\infty = 13.6$ m/s, pressure, p_∞ and the air density, ρ and viscosity, μ, resulting in a Reynolds number of $Re = \rho h u_\infty/\mu \simeq 65000$. The base blowing was injected with an air flow rate of q_b, expressed in dimensionless form as $C_q = q_b/(u_\infty wh) \in [0, 0.0315]$, through four configurations with slots of different geometries: square (**S**), cross (**C**), vertical (**V**) and horizontal (**H**) slots, shown in Fig. 1(c) alongside the baseline case (**B**). The aerodynamic force coefficients are obtained as $c_i = 2(f_i - f_{i,b})/\rho u_\infty^2 hw$ with $i = [x, y]$, where f_i and $f_{i,b}$ represent respectively the aerodynamic forces acting in the body and the thrust forces caused by the blowing system alone. The pressure measurements at the tap j are made non-dimensional using pressure coefficients, defined as $c_{p,j} = \frac{1}{n}\sum_{i=1}^{n_a} 2(p_j - p_\infty)/\rho u_\infty^2$. Thus, the base drag coefficient, c_B, is also computed as $c_B = -\sum_{j=1}^{n_a} c_{p,j}$ where n_a is the total number of the base pressure taps available. Additionally, horizontal base pressure gradient, g_y, can be calculated as $g_y = h\frac{\partial c_p}{\partial y} \simeq h(\sum^{n_{al}} c_{p,j} - \sum^{n_{ar}} c_{p,j})/2(y_l - y_r)$ where $(y_l - y_r)/h = 1$ is the horizontal distance between the left and right columns of base pressure taps. The variables n_{al} and n_{ar} represent all the respective available locations of the left and right columns of taps, represented in purple in Fig. 1(a). In the following, time-dependent variables will be denoted using lower-case letters a, while time-averaged values will be expressed by means of upper-case letters $A = \overline{a}$.

Figure 2(a, b, c) shows the variations of the averaged base drag coefficient, ΔC_B^k, drag coefficient, ΔC_x^k, and the recirculation bubble length, ΔL_r^*, with respect to the baseline case (**B**) values. The recirculation region length, $L^* = L_r/H$, is defined as the streamwise distance between the body base (located at $x = 0$) and the furthest point of the recirculation separatrix in x, given by the streamlines of the mean flow.

Similar trends are observed for all configurations when the blowing is activated, namely: an initial decrease of the coefficients followed by a subsequent increase given at large blowing coefficient, thus defining two mass and momentum regimes (see Fig. 2). The mass regime results then into base pressure recovery with the increasing blowing, which is caused by the inflation of the recirculation region. The drag reduction trends are similar for the tested blowing configurations. Conversely, over the momentum regime, the base pressure is reduced and the drag increases with increasing blowing, due to the high momentum jet produced at the blowing slot. While the mas regime depicts similar trends for all configurations, these of momentum regime are seen to be highly dependent on the slot geometry. Thus, among the different tested cases, the **S** slot is the most efficient configuration since it provides the larges drag reduction, ΔC_x, followed by the **H** slot. Configurations with vertical slots, i.e. (**C** and **V**), are shown to be the least efficient configurations. This hierarchy is based on the efficiency of the blowing configuration in lengthening the recirculation region without disturbing the near wake.

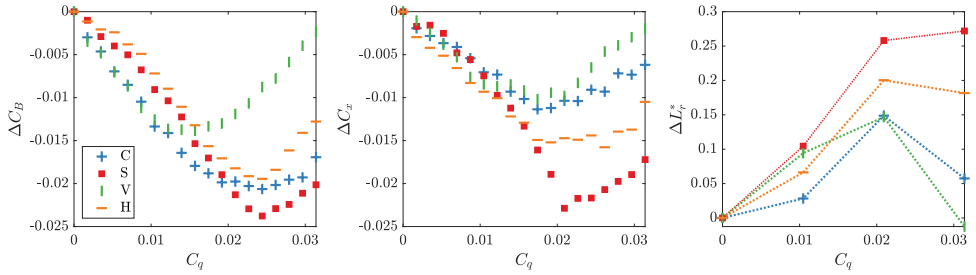

Figure 2: Evolution of averaged (a) base drag coefficient, ΔC_B, (b) drag coefficient, ΔC_x, and (c) recirculation bubble length, ΔL_r^*, variations with respect to **B** case at different blowing flow rates, C_q.

On the other hand, the reference wake exhibits initially a quasi-static asymmetry attributed to the presence of the Reflectional-Symmetry-Breaking (RSB) mode [3]. The blowing affects however this topology. The RSB mode sensitivity to blowing geometry is shown in Fig. 3. Here, the most effective slot for drag reduction, **S**, also manages to symmetrize the wake [4]. On the other hand, the least efficient blowing configurations, **V** and **C**, lead to increased wake asymmetry as blowing flow rates C_q rise.

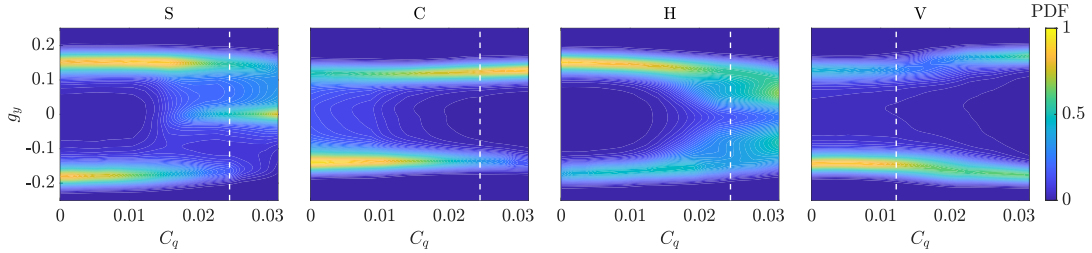

Figure 3: Probablity Density Functions (PDFs) of the horizontal base pressure gradient, g_y, for the different blowing configurations (**S**, **C**, **V** and **H**) at the tested blowing flow rates, C_q. Dashed white lines represent the blowing flow rate that recovers the maximum base pressure for each configuration.

This work is a result of the Projects TED2021-131805B-C21 and TED2021-131805B-C22, financed by the Spanish MCIN/AEI/10.13039/501100011033/ and the European Union NextGenerationEU/PRTR.

References

[1] H. Choi, J. Lee, and H. Park. Aerodynamics of heavy vehicles. *Annu. Rev. Fluid Mech.*, 46 (1):441–468, 2014.

[2] M. Lorite-Díez, J. I. Jiménez-González, L. Pastur, C. Martínez-Bazán, and O. Cadot. Experimental sensitivity analyses of modes to blowing at the base of a 3D bluff body. *J. Fluid Mech.*, 883:A53, 2020b.

[3] M. Grandemange, M. Gohlke, and O. Cadot. Turbulent wake past a three-dimensional blunt body. Part 1: Global modes and bi-stability. *J. Fluid Mech.*, 722:51–84, 2013.

[4] T. I. Khan, V. Parezanović, L. Pastur, and O. Cadot. Suppression of the wake steady asymmetry of an ahmed body by central base bleed. *Phys. Rev. Fluids*, 7(8):083902, 2022.

Experimental passive control of the Ahmed body without ground effect using deflectors at a low Reynolds number

Pedro Solis[*], José Antonio Santiago[*], Eduardo Duran[*], Carlos del Pino[*]

Abstract We have conducted an experimental investigation on the effect of different deflector angles on the drag and lift coefficients of an Ahmed body without ground effect. Our findings show that the minimum drag corresponds to a deflector angle between -4 and 0°.
Keywords: aerodynamics, passive control, bluff body.

Improving the reduction of aerodynamic drag is one of the main tasks in engineering to reduce fuel consumption in ground or air vehicles. Although the geometry of the vehicles is already highly optimized, this is not the case for heavy vehicles such as trucks or buses. Researchers apply different passive and active flow control techniques to reduce aerodynamic drag [1]. Most of these techniques deal with the massive flow separation at the rear of vehicles, where two main flow structures are the origin of drag sources: one recirculation bubble and one pair of longitudinal counter-rotating vortices (C-vortices) [2]. The former causes pressure to drop at the rear, and the latter is a source of (aerodynamic) induced drag [3].

We measured the hydrodynamic forces and the wake velocity fields generated by an Ahmed body model (rear slant angle of 25°, length L=221 mm) with no ground effect using different deflector angles (α) to reduce the drag. We obtained velocity measurements from 2D-PIV in a plane perpendicular to the free-stream direction. We conducted the experiments in a towing water tank at a constant height-based Reynolds number, $Re_H = 20 \times 10^3$. We present the average results over a set of three experiments.

Drag force measurements, see figure 1 (a), show that the maximum drag reduction occurs for α values between -4° and 0°, diminishing the drag up to approximately 12% respect to the base case. This reduction is maintained of the same order of magnitude up to $\alpha \approx -8°$. However, for very low angles, the drag increases approaching the base case value, $\alpha \to -25°$. For positive values of α, despite the bigger projected area, the drag does not overcome the configuration without deflector until $\alpha = 16°$. Additionally, the deflector always reduces the lift respect to the base case, as shown in figure 1 (b). We also observe that lift decreases as α increases, and at the minimum drag configuration, it drops to less than half of the base case. This reduction is a desirable effect since lift reduces the traction of the tyres on ground vehicles and results in an increased risk of skidding.

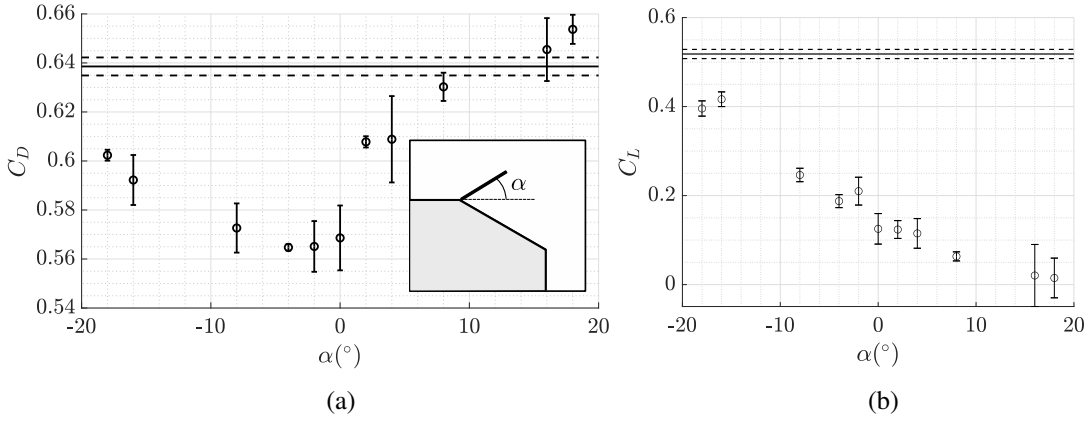

Figure 1: Drag (a) and lift (b) coefficients and its standard deviation versus α. Continuous and dashed lines represent the base case. The inset in (a) shows a scheme of the rear of the model with the deflector.

The drag measurements can be related to the wake vorticity. We focus on analyzing three relevant cases: the

[*]Fluid Mechanics, University of Málaga, Institute for Mechatronics Engineering & Cyber-Physical Systems , Málaga, Spain

model with no deflectors, the minimum drag configuration ($\alpha = -4°$), and a high drag configuration ($\alpha = 16°$). The streamwise component of the vorticity (ω) is mainly generated by the longitudinal (streamwise) vortices. The integral of ω over the measurement plane results in almost zero net circulation since the vorticity alters signs for counter-rotating vortices. Therefore, we integrate the absolute value of ω to estimate the C-vortices strength (see figure 2). The case with $\alpha = -4°$ displays lower values, suggesting a drop in the induced drag as a cause of the total drag reduction.

Furthermore, the weakening of the C-vortices is also evident when looking at the vorticity and velocity in a (X, Y)-plane, as shown in figure 3. The structure of the counter-rotating vortices is easily identifiable for the base case (a) but not for $\alpha = -4°$ (b), which has a less coherent wake structure. Furthermore, the degeneration of the C-vortices seems to cause a reduction of the downwash, which may be associated with a reduction of the lift.

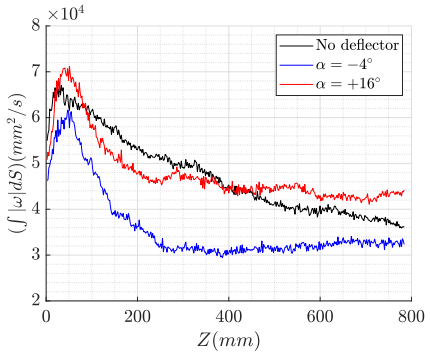

Figure 2: The absolute value of the streamwise component of the vorticity integrated over the measurement plane as a function of the streamwise direction Z from the model vertical origin at the trailing edge.

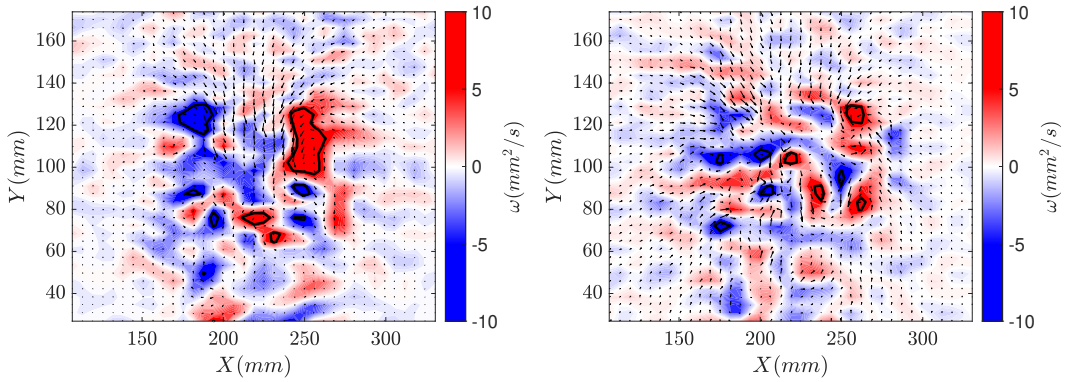

Figure 3: Velocity field (arrows) and vorticity fields (heatmap) at a distance z=10mm to the vertical base for (a) no deflector and (b) $\alpha = -4°$. ω=7mm^2/s level marked in black lines.

References

[1] Hung, T. T., Hijikuro, M., Anyoji, M., Uchida, T., Nakashima, T., & Shimizu, K. *Deflector effect on flow behavior and drag of an Ahmed body under crosswind conditions*, Journal of Wind Engineering and Industrial Aerodynamics, **231**, 105238. (2022).

[2] Tran, T. H., Hijikuro, M., Anyoji, M., Uchida, T., Nakashima, T., & Shimizu, K. *Surface flow and aerodynamic drag of Ahmed body with deflectors*, Experimental Thermal and Fluid Science, **145**, 110887 (2023).

[3] Choi, H., Lee, J., & Park, H. *Aerodynamics of heavy vehicles*, Annual Review of Fluid Mechanics **46**, 441-468 (2014).

EXPLORING WAKE DYNAMICS INTERACTION WITH REAR FLEXIBLE FLAPS ON A SQUAREBACK AHMED BODY

J.C. Muñoz-Hervás[1,2], M. Lorite-Díez[2,3], C. García-Baena[1,2], J.I. Jiménez-González[1,2]
[1]*Dpto. de Ingeniería Mecánica y Minera. Universidad de Jaén, Jaén, Spain.*
[2]*Instituto Interuniversitario de Investigación del Sistema Tierra en Andalucía. Universidades de Granada, Jaén and Córdoba, Spain.*
[3]*Dpto. de Mecánica de Estructuras e Ingeniería Hidráulica. Universidad de Granada, Granada, Spain.*
Contact: jcmunoz@ujaen.es.

The bluff geometry of heavy vehicles contributes to a significant aerodynamic drag, partly caused at their blunt base where flow separation occurs. Several studies have proposed rear devices to act on the near wake and consequently, to reduce the aerodynamic drag, as e.g. rigid cavities [1]. However, conventional rigid passive systems may not always perform optimally under changing flow conditions, such as transient flow or crosswinds [3]. Alternatively, the use of flexible self-adaptive solutions, that can passively modify their geometry to changing near wake features, may overcome these limitations, offering an efficient solution to reduce drag under different flow conditions.

Following this approach, we conducted wind tunnel experiments to analyze the wake behind a square-back Ahmed body. The model of height $H = 72$ mm, length $L = 4.04H$, and width $W = 1.35H$ (see Fig.1), was subjected to uniform flow of free-stream velocity u_∞, density ρ_f, and viscosity μ_f. The Reynolds number $Re = \rho_f u_\infty H/\mu_f$ ranges from $5 \cdot 10^4$ to $9 \cdot 10^4$. For these experimental conditions, the wake behind the model exhibit quasi-static asymmetry, induced by the destabilization of Reflectional-Symmetry-Breaking (RSB) mode [2], which governs the drag reduction mechanisms. As self-passive device, we employed two flexible brass foils, each with a length of $B = 0.46H$, attached at the base edges that can be deformed in 2D (see Top view on Fig.1). We measured the base pressure (p_j), the aerodynamic forces (f_i), the near wake features by planar PIV (u_x, u_y) and the flaps deformation (θ) with a high-speed camera. We compared three different configurations: (1) the reference baseline case (REF), (2) rigidly mounted flaps, with the same length as the employed flexible flaps (RF), and (3) the described flexible flaps (FF). To evaluate the effect of the passive devices under crosswind conditions, we set three different yaw angles: $\beta = 0°, 5°, 10°$. We assessed the fluid-structure interaction between the flexible flap and the wake behind the Ahmed body by varying the Cauchy number, $Ca = \rho_f u_\infty^2 HB^3/2EI$, in a range of [16.8, 53.2]. In the following, time-dependent variables will be denoted using lower-case letters a, while time-averaged values will be expressed by means of upper-case letters $A = \overline{a}$.

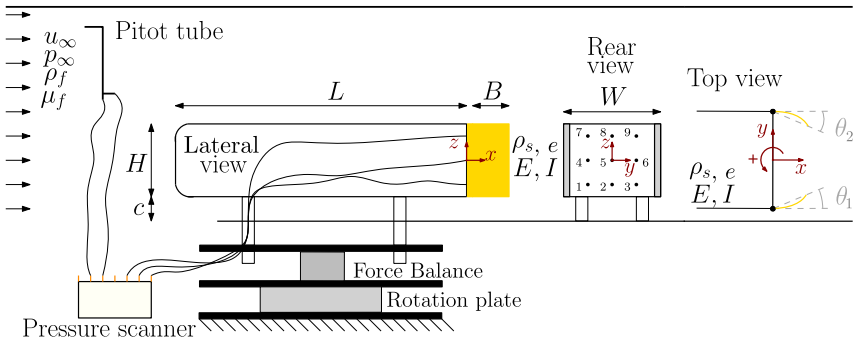

Figure 1: Sketch of the experimental set-up.

To observe the effect of the flexible and rigid flaps on the drag coefficient, $C_x = F_x/0.5\rho_f u_\infty^2 HW$, we have computed the relative difference between the values obtained for the two flap configurations (rigid, RF, and flexible, FF) and the baseline case (REF). In Fig. 2(a), it can be noticed that the rigid flaps slightly reduce the drag for aligned conditions. However, an increase in this coefficient is observed for non-aligned conditions, presumably due to the appearance of streamwise vortices. For the flexible flaps case, a significant reduction in drag is observed not only for aligned conditions but also for yawed conditions, owing to the flaps' self-adaption to the flow, particularly for low Ca values. In that regard, Fig. 2(b) shows the time-averaged angular deflection of the flap tips, Θ. At low Ca, the flexible flaps undergo an , inwardly, quasi-static passive reconfiguration (see Fig. 2c, top) for all tested angles, resulting in reduction of the drag. At large Ca values, there is a sudden increase of the reconfiguration mean angle alongside with important flaps vibrations (see Fig. 2c, bottom) which is detrimental in terms of drag. This large

amplitude flap vibrations are related to the appearance of high-deformation mode in the flexible flap. The threshold in terms of value of Ca depends on the yaw angle, B. For example, at $\beta = 5°$, the angle of the windward flap, Θ_2, starts to oscillate vigorously at smaller Ca values than the leeward flap, Θ_1, which remains under quasi-static passive reconfiguration at $Ca \simeq 43$.

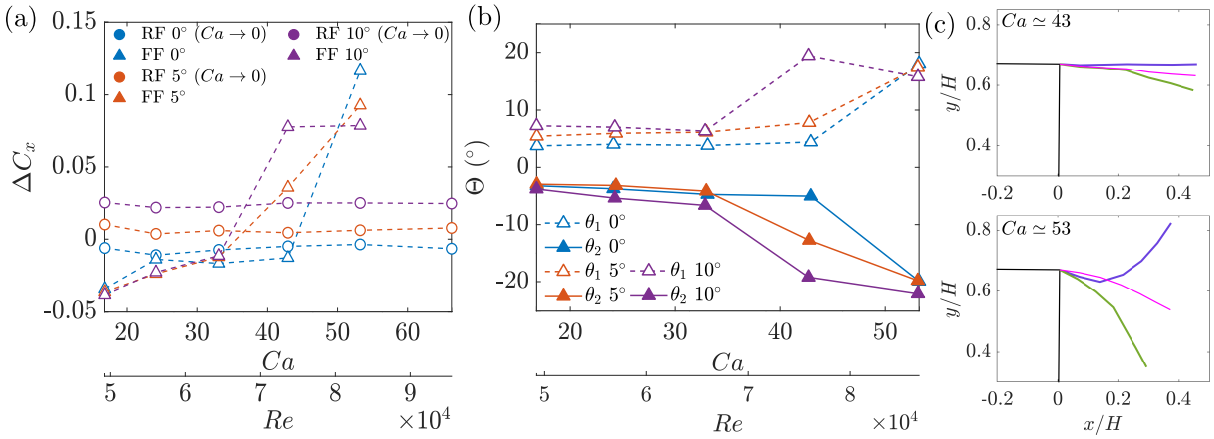

Figure 2: Evolution of (a) the relative drag coefficient and (b) the averaged flap deflection angle, Θ, with Ca (or Re) under the different tested yaw angles and configurations. (c) Instantaneous (in blue and green) and averaged (in pink) flap deformations at $Ca \simeq 43$ (top) and $\simeq 53$ (bottom).

The drag reduction achieved by the flaps is a result of the interaction between the flaps and the near wake, as depicted in Fig. 3 by time-averaged streamwise velocity, U_x, contours alongside averaged flow streamlines (U_x, U_y). For the baseline case (see Fig. 3a), a symmetric recirculation bubble is observed, despite the presence RSB mode, which indicates an equal probability of exploration for both horizontally deflected wake states. When rigid flaps are set (see Fig. 3b), an elongation of the recirculation bubble occurs due to the increased distance between the recirculation region cores and the body base caused by the flaps, leading to pressure recovery at the base and the suppression of the RSB mode [1]. For flexible flaps (see Fig. 3c), the flaps produce some wake shaping, justifying the observed pressure recovery at the base and hence, drag reduction, C_x.

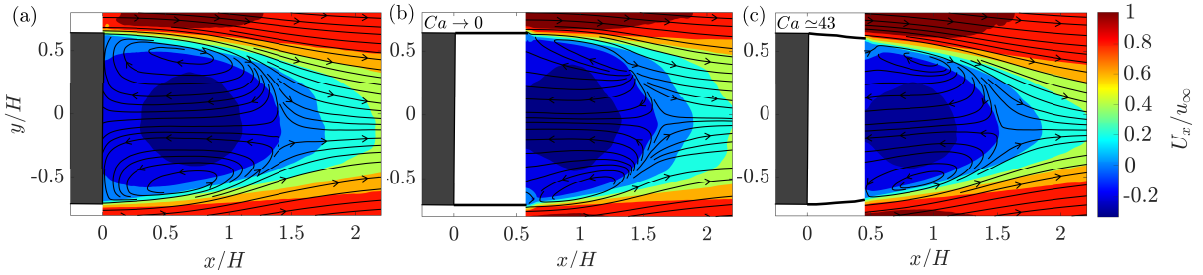

Figure 3: Time-averaged flow at the horizontal plane placed at $z = 0$ for: (a) baseline case, (b) rigid flaps at $Re \simeq 77000$ and (c) flexible flaps at $Ca \simeq 43$ ($Re \simeq 77000$).

This work is a result of the Projects TED2021-131805B-C21 and TED2021-131805B-C22, financed by the Spanish MCIN/AEI/10.13039/501100011033/ and the European Union NextGenerationEU/PRTR.

References

[1] A. Evrard, O. Cadot, V. Herbert, D. Ricot, R. Vigneron, and J. Délery. Fluid force and symmetry breaking modes of a 3D bluff body with a base cavity. *J. Fluids Struct.*, 61:99–114, 2016.

[2] M. Grandemange, M. Gohlke, and O. Cadot. Turbulent wake past a three-dimensional blunt body. Part 1: Global modes and bi-stability. *J. Fluid Mech.*, 722:51–84, 2013.

[3] M. Lorite-Díez, J. I. Jiménez-González, L. Pastur, O. Cadot, and C. Martínez-Bazán. Drag reduction on a three-dimensional blunt body with different rear cavities under cross-wind conditions. *J. Wind Eng. Ind. Aerod.*, 200:104145, 2020a.

Exploring the effects of spanwise wing deformation on lift coefficient and trailing vortices properties at low Reynolds number

Manuel Garrido-Martin*, Pedro Solis*, Eduardo Duran*, Paloma Gutierrez-Castillo*, and Carlos del Pino*

Abstract We have conducted an experimental investigation on the effect of spanwise wing deformation on the lift coefficient and the properties of the wingtip vortices generated by several NACA0012 symmetric wing models.
Keywords: wingtip vortex, aerodynamics, flow visualization, wing model deformation.

The state-of-the-art research on steady-state aerodynamics under subsonic flow conditions presents a wide variety of studies that contemplate the characterization and analysis of flight conditions with rigid wing models. However, the advent of increasingly lighter airfoil materials causes considerable spanwise deformations, which has become a relevant concern for the operation at low Reynolds number regimes of Micro Air Vehicles (MAVs) and Unmanned Aerial Vehicles (UAVs). The flow dynamics at this regime are notably intricate, primarily driven by a laminar separation bubble (LSB) developed on the suction side of the wing profiles. Consequently, even subtle changes in experimental conditions or wing geometry can significantly impact wing forces and wake flow structures, which are critical in determining the optimal active control of the fluid flow.

We have measured both the hydrodynamic forces and the velocity fields generated in the wake of three different NACA 0012 rigid wing models for several angles of attack lower than the stall value in a towing water tank located in the Laboratory of Aero-Hydrodynamics of the University of Málaga, Spain. We conducted all experiments at the same chord-based Reynolds number, $Re = 20 \times 10^3$, and each of the three wing models considered presents a varying level of spanwise deformation: non-deformed (ND), intermediate deformation with a tip deflection of $\delta = 2\%$ (ID) and large deformation with a tip deflection of $\delta = 4.5\%$ (LD). We show in Figure 1 a graphic visualization of the deflection curves along the spanwise direction for these models.

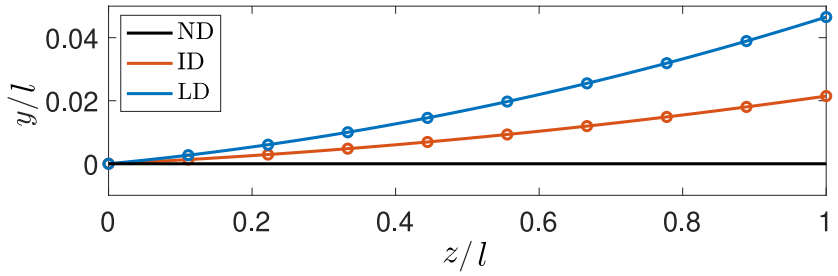

Figure 1: Non-dimensional spanwise deflection levels, extracted from experimental measurements(1): non-deformed (ND, $\delta = 0\%$), intermediate deformation (ID, $\delta = 2\%$), and large deformation (LD, $\delta = 4.5\%$).

Force measurements reveal three discernible zones within the range of angles of attack investigated, each presenting different lift slopes. These zones persist even for the deformed wings, indicating consistent aerodynamic behavior across different wing configurations. One initial observation is that at lower angles of attack, for instance, $\alpha = 4^\circ$, the non-deformed wing configuration exhibits higher lift than the maximum spanwise deformed wing. Conversely, at higher angles of attack, such as $\alpha = 8^\circ$, the spanwise deformed wing configuration presents a higher lift. These changes in the lift forces for different spanwise deformations can be observed in Figure 2 (a).

*Universidad de Málaga, Institute for Mechatronics Engineering and Cyber-Physical Systems (IMECH.UMA), Campus de Teatinos, s/n, 29071 Málaga, Spain

Additionally, the deformation decreases the circulation over the wing for $\alpha < 6$ concerning the circulation of non-deformed values and increases it for greater α, as observed in Figure 2 (b). This tendency change is also directly related to the circulation measured in a plane perpendicular to the wing model movement, as proposed in (3). We have shown that their empirical relationship between the circulation over the wing due to lift vortex (obtained from C_L) and the circulation measured in a plane perpendicular to the wing model movement (computed from 2D-PIV experimental measurements) is valid for our study.

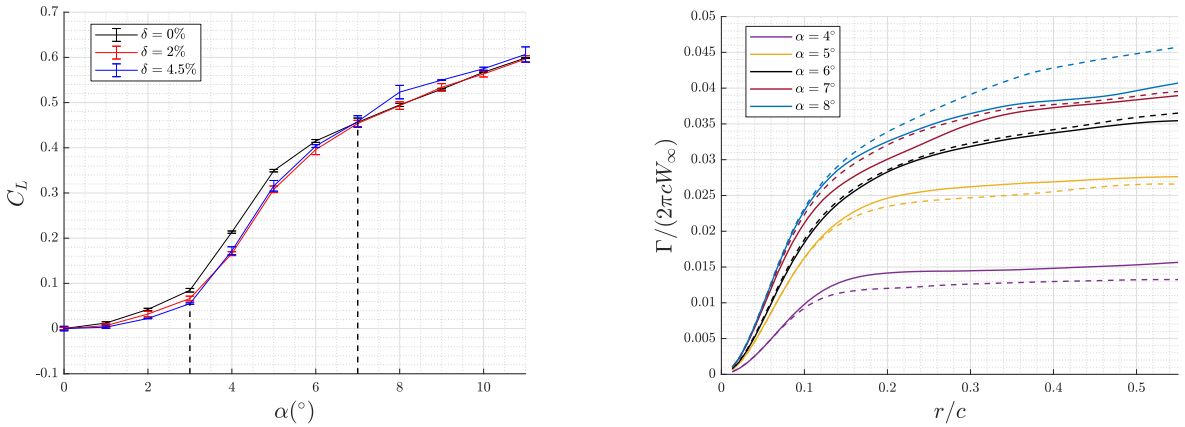

(a) (b)

Figure 2: (a) Lift coefficient versus the angle of attack for three different levels of deformation, and (b) circulation with respect to the radial coordinate for 5 different angles of attack, where solid lines represent non-deformed wings and dashed lines represent deformed wings with $\delta = 4.5\%$. Figures extracted from (2).

References

[1] Farnsworth, J. A., Corbett, S., Seidel, J., and McLaughlin, Thomas E. *Aeroelastic Response of a Finite Span NACA 0018 Wing Part 1: Experimental Measurements*, 53rd AIAA Aerospace Sciences Meeting, 0249 (2015).

[2] Solis, P., Garrido-Martin, M., Duran, E., Gutierrez-Castillo, P. and del Pino, C. *On the influence of spanwise deformation on lift coefficient and trailing vortices properties at low Reynolds number*, Physics of Fluids **36(3)**, 037122 (2024).

[3] Xu, M., Cheng, H., Ji, B., and Peng, X. *Prediction method of tip vortex circulation based on hydrofoil load*, Ocean Engineering **288**, 116176 (2023).

Stall Flutter Characteristics of a Pitching NACA 63(3)418 Aerofoil with Passive Camber Morphing Capabilities

City, University of London
Quentin Martinez, Chetan Jagadeesh, Mohammad Omidyeganeh

Motivation

Fatigue related downtime in offshore wind farms continues to be an important logistical and financial consideration despite continued growth in wind turbine efficiency and aggregate power output. Some authors have estimated between 4-10% average downtime for offshore wind turbines (Horn and Leira, 2019) due to a combination of electrical and mechanical failures. Kolios and Cevasco (2021), reported an appreciably larger downtime range, 0.9-19.8%, based on a comprehensive survey of various reliability studies in Europe (Cevasco, Koukoura, and Kolios, 2021). They also note a disparity in operational availability between mega-watt range, off and onshore wind turbines (onshore being less susceptible to failure) supported by a prior correlation of turbine failure rate and unfavourable environmental conditions (Tavner et al., 2012). To broaden the mechanical lifetime of offshore wind turbines, current research has been focused towards fatigue mitigation by means of active and passive flow control mechanisms. The primary goal of these devices is to assist in load alleviation during transient conditions like gusts, crosswinds, or wakes. One promising method to achieve such alleviation is by using compliant aerofoil profiles that can adapt their camber in response to aerodynamic loading. A similar moderating effect can be achieved by a hinged flap that also acts to passively adjust camber.

Introduction

Significant load alleviation for fatigue susceptible aeroelastic structures like wind turbine blades has been demonstrated to be possible by the inclusion of passive camber morphing capabilities (Cordes et al., 2018), (Bak et al., 2007), (Bottasso et al., 2016) where an elastic response to coupled inertial, structural, and aerodynamic forces can help attenuate cycle-per-cycle load variations. At high mean angles of attack though, transient environmental conditions can provoke perturbations beyond the static stall angle where the periodic shedding/reattachment of flow may lead to pronounced load variations and hysteresis effects. This has motivated additional interests in camber morphing technology as a potential suppressant to the dynamic stall process. In this context, there has been a significant amount of work conducted on active camber morphing devices and their role on fatigue lifetime for high mean angle of attack conditions. Wu et al. (2023) demonstrated a decrease in pitching moment variation for a prescribed dynamic stall process by using a spanwise deformable flap. Samara and Johnson (2020) also showed significant load alleviation for a prescribed pitching aerofoil section by means of a hinged flap. Seyednia, Masdari, and Vakilipour (2019) and Zhuang et al. (2020) both demonstrated similar load control capabilities for lift and drag forces on a pitching aerofoil section via camber morphing. It is worth emphasizing that all these particular cases implemented prescribed pitching and flap motions which is different from a purely passive aeroelastic system. In general, though, the trailing edge flap chord fraction, amplitude of flap deflection and phase offset between rigid body and flap motion all significantly contribute to the manipulation of aerodynamic loads during the dynamic stall process. Some of the mentioned authors also demonstrated how specific phase offsets can lead to enhanced energy extraction from the incoming free stream. More specifically, there exists a potential range of phase offset conditions between the rigid body and deforming flap motion that promote negative aerodynamic damping and therefore the instability state known as stall flutter. While this circumstance of camber morphing aerofoils has been speculated in prior works, there is no significant body of literature investigating such an instability for a wing or aerofoil section with passive camber morphing capabilities through high fidelity simulations or experimental techniques. Thus, the current project aims to provide both a quantitative and phenomenological characterisation of the stall flutter instability for a camber morphing NACA 63(3)418 aerofoil.

Methodology

The current workload consists of simulating the pitch degree of freedom stall flutter instability with passive trailing edge via high-fidelity large eddy simulations (SUSA) (Rosti et al., 2016). Simulated results will be validated

through stereoscopic Particle image velocimetry (PIV), aerodynamic moment measurements, and pitch position optical encoder measurements. Both simulated and experimental results will also be compared to rigid body measurements to inform how passive camber morphing devices either attenuate or exaggerate the stall flutter instability at similar operating conditions. All CFD based results are computed using an in-house, incompressible, Navier-Stokes solver on structured grids. The current version implements the finite-volume method and fractional step temporal discretisation that is parallelised using the MPI message passing library. All experimental results are measured in City, University of London's subsonic T2 wind tunnel facility with modifications to include a cyber-physical aerofoil pitching system. The designed cyber-physical system is based on a similar approach by Fagley, Seidel, and McLaughlin, (2015), Farnsworth and Culler, (2019), and Hover et al., (2000) where a feedback control system is used to prescribe a motor torque response that emulates a torsion spring, mass, damper system. In this formation, cyber-physical control gains representing spring stiffness, moment of inertia, and damping can be adjusted to vary the stall flutter bifurcation conditions and oscillatory response of a pitching aerofoil. Progress to date primarily regards CFD and wind tunnel testing of the NACA 63(3)418 aerofoil section under static conditions for baseline data at low chord-based Reynolds numbers. CFD simulated results shows good agreement with static load wind tunnel measurements up to high angle of attack conditions ($\alpha = 10°$) at Re=100,000. Beyond the linear aerodynamic regime though, we observe a departure from predicted lift and drag measurements. Passive tufts on the aerofoil suction side also provide good qualitative agreement on the flow separation front as it traverses the chordwise direction from trailing edge to leading edge. Preliminary flutter simulations for a rigid body aerofoil section clearly demonstrate a loading hysteresis effect due to leading edge vortex formation, propagation, shedding, and flow reattachment. Cycle-to-cycle aerodynamic moment profiles also confirm the presence of energy extraction which indicates an incomplete but necessary condition for sustained limit cycle oscillations. Future work consists of testing the cyber-physical control system for pitching responses to small perturbations and comparison with CFD results over a range of reduced frequencies.

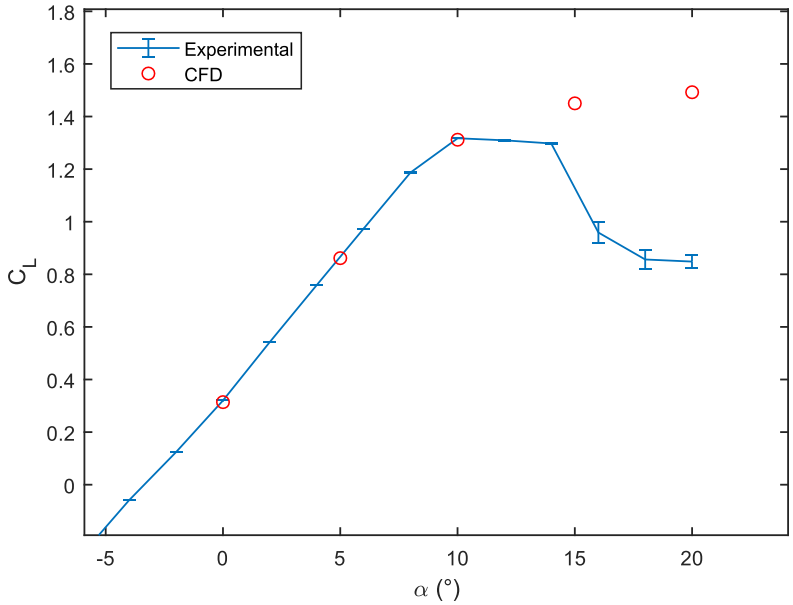

Figure 1. Static lift polar experimental (blue) versus CFD comparison (red)

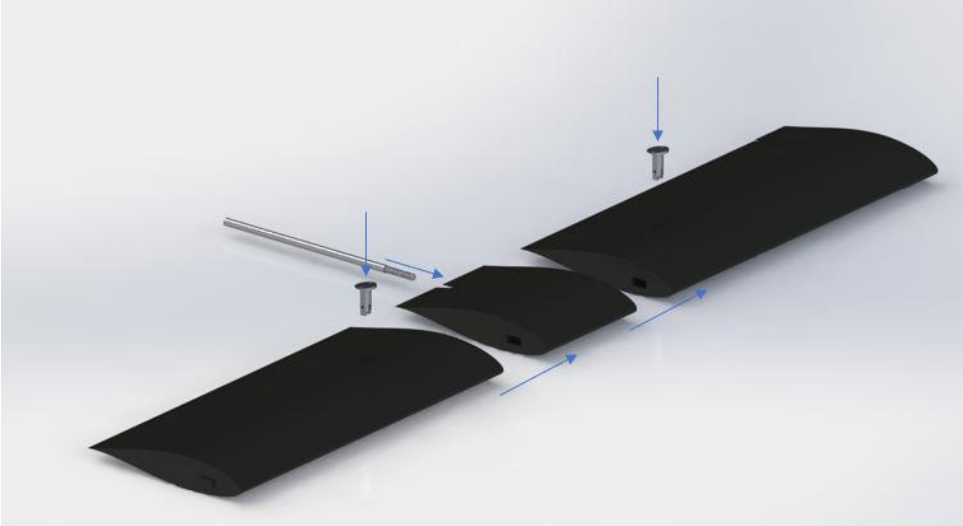

Figure 2. NACA 63(3)418 aerofoil mounting assembly render

Bibliography

Bak, C. *et al.* (2007) 'Wind tunnel test on wind turbine airfoil with adaptive trailing edge geometry', *45th AIAA Aerospace Sciences Meeting and Exhibit* [Preprint]. doi:10.2514/6.2007-1016.

Bottasso, C.L. *et al.* (2016) 'Load mitigation for wind turbines by a passive aeroelastic device', *Journal of Wind Engineering and Industrial Aerodynamics*, 148, pp. 57–69. doi:10.1016/j.jweia.2015.11.001.

Cevasco, D., Koukoura, S. and Kolios, A.J. (2021) 'Reliability, availability, maintainability data review for the identification of trends in offshore wind energy applications', *Renewable and Sustainable Energy Reviews*, 136, p. 110414. doi:10.1016/j.rser.2020.110414.

Cordes, U. *et al.* (2018) 'The Adaptive camber concept—A passive approach for gust load alleviation on wind turbines', *Wind Energy*, 21(9), pp. 732–744. doi:10.1002/we.2190.

Culler, E.C.E. and Farnsworth, J.A.N. (2019) 'Higher frequencies in stall flutter moment development', *Journal of Fluids and Structures*, 85, pp. 181–198. doi:10.1016/j.jfluidstructs.2019.01.007.

Fagley, C.P., Seidel, J. and McLaughlin, T.E. (2015) 'Experimental investigation of the aeroelastic behavior a NACA0018 cyber-physical flexiblewing', *33rd AIAA Applied Aerodynamics Conference* [Preprint]. doi:10.2514/6.2015-2251.

Horn, J.-T. and Leira, B.J. (2019) 'Fatigue reliability assessment of offshore wind turbines with stochastic availability', *Reliability Engineering & System Safety*, 191, p. 106550. doi:10.1016/j.ress.2019.106550.

Hover, F.S. and Triantafyllou, M.S. (2000) 'Combined simulation with real-time force feedback: A new tool for Experimental Fluid Mechanics', *The Kluwer International Series in Engineering and Computer Science*, pp. 463–474. doi:10.1007/978-1-4615-5223-9_33.

Rosti, M.E., Omidyeganeh, M. and Pinelli, A. (2016) 'Direct numerical simulation of the flow around an aerofoil in ramp-up motion', *Physics of Fluids*, 28(2). doi:10.1063/1.4941529.

Samara, F. and Johnson, D.A. (2020) 'Dynamic stall on pitching cambered airfoil with phase offset trailing edge flap', *AIAA Journal*, 58(7), pp. 2844–2856. doi:10.2514/1.j059115.

Seyednia, M., Masdari, M. and Vakilipour, S. (2019) 'The influence of oscillating trailing-edge flap on the dynamic stall control of a pitching wind turbine airfoil', *Journal of the Brazilian Society of Mechanical Sciences and Engineering*, 41(4). doi:10.1007/s40430-019-1693-z.

Tavner, P.J. *et al.* (2012) 'Study of weather and location effects on wind turbine failure rates', *Wind Energy*, 16(2), pp. 175–187. doi:10.1002/we.538.

Wu, Y. *et al.* (2023) 'Effect of spanwise distributed camber morphing on dynamic stall characteristics of a finite-span wing', *Physics of Fluids*, 35(10). doi:10.1063/5.0168549.

Zhuang, C. *et al.* (2020) 'Effect of morphed trailing-edge flap on aerodynamic load control for a wind turbine blade section', *Renewable Energy*, 148, pp. 964–974. doi:10.1016/j.renene.2019.10.082.

Reinforcement Learning of Active Aerodynamics in Wind Tunnel Environments

Georgios Rigas[1]

[1] Imperial College London, Department of Aeronautics, London SW7 2AZ, UK
g.rigas@imperial.ac.uk
www.imperial.ac.uk/people/g.rigas

I will discuss our recent progress on applying Reinforcement Learning (RL) to intractable turbulent fluid flow systems for optimising the aerodynamic efficiency through flow control and accelerating the transition to Net Zero. Since the governing fluid-flow equations are intractable for simulated environments for realistic geometries and high Reynolds numbers turbulent regimes, we apply RL in real time/real environments by interacting with the wind tunnel environment, which consists of a car model, dynamic actuators for aerodynamic shaping, and wall mounted pressure sensors. Our goal is to discover dynamic wake control strategies that minimise the aerodynamic drag.

From an algorithmic perspective, I will discuss challenges associated to partial observability, convergence, and delays. A thorough analysis will be presented using simpler configurations before deploying them in the wind-tunnel environment. At laminar and two-dimensional flow regimes, the performance of the RL under partial observability of the flow dynamics (pressure sensors on the body) is significantly degraded, limiting drag reduction by 50% compared to probes optimally located downstream of the body. A method integrating memory into the control architecture is proposed to improve performance in partially observable systems. By augmenting the input to the controller (neural network) with a time series of lagged observations from past actions and sensors, the dynamic controllers discovered using RL completely stabilise the vortex shedding using only surface mounted sensors.

From a hardware perspective, I will discuss efficient implementation of RL algorithms for real-time training and preliminary results from wind tunnel experiments of RL for road vehicle drag reduction. These results are a first step towards realistic implementation of reinforcement learning for optimising partially observable and intractable flows.

Acknowledgements: This work is supported by the UKRI AI for Net Zero grant (EP/Y005619/1).

REFERENCES

[1] C. Xia, J. Zhang, E. C. Kerrigan, and G. Rigas, Active Flow Control for Bluff Body Drag Reduction Using Reinforcement Learning with Partial Measurements. *J. Fluid Mech.*, 981, 2024.

[2] Max Weissenbacher, Anastasia Borovykh, Georgios Rigas, CHAROT: Robustly controlling chaotic PDEs with partial observations. ICLR, 2024.

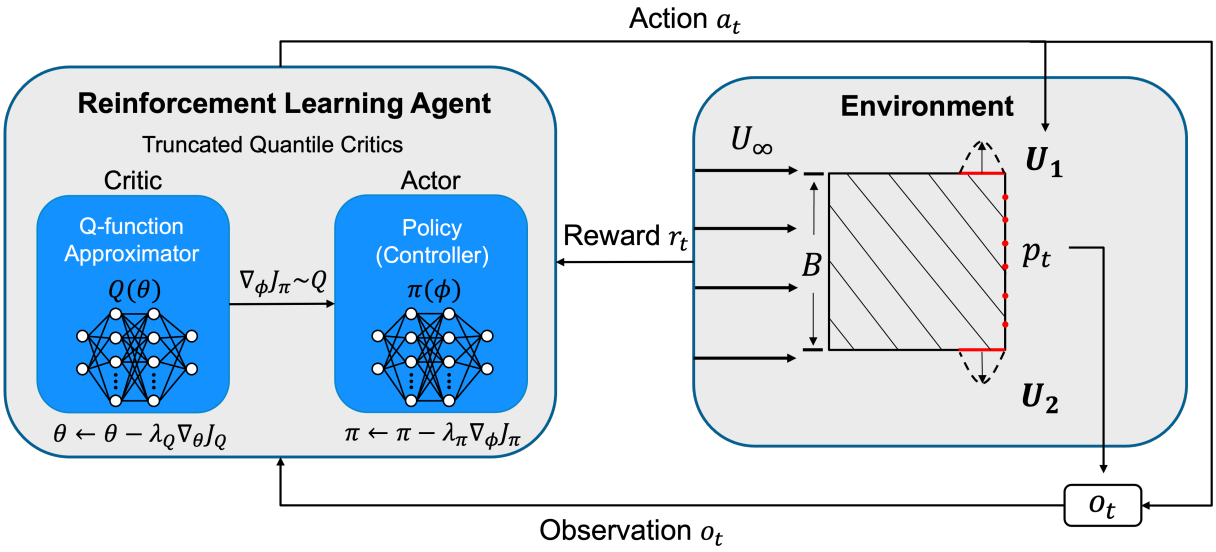

Figure 1: Schematic of the Reinforcement Learning setup for discovering optimal dynamic control strategies to stabilise the unsteady wake and reduce the aerodydamic drag.

From on-road experiments to active closed loop control of base drag variations for slowly varying upstream flow conditions.

Agostino Cembalo[a,c], Jacques Borée[a], Patrick Coirault[b,*] , Clément Dumand[c]

a) Pprime Institute CNRS, ENSMA, University of Poitiers, 1 Av. Clément Ader, 86360, Chasseneuil, France
b) Laboratory LIAS - ENSIP, University of Poitiers, 2 rue Pierre Brousse, 86073, Poitiers, France
c) STELLANTIS, Advanced Innovation, 212 Bd Pelletier, Carrières-sous-Poissy, 78955, France

ABSTRACT

The growing focus on reducing energy consumption, particularly for electric vehicles with limited autonomy, has prompted innovative solutions. In real-life scenarios, i.e. the variety of operating conditions that any vehicle has to face over his life cycle, the vehicle is subject to continuous inputs from the natural wind and the wake of other vehicles. Lot of studies have been devoted to characterizing the effects of changes in the surrounding environments. Using quasi-steady approaches, a wind averaged drag coefficient can be defined using representative wind-speed distributions (Howell et al. 2017). This wind averaged drag coefficient is significantly higher than the basic drag coefficient at zero yaw. As stressed by these authors, reducing the sensitivity of the aerodynamic loads to the natural wind is therefore a critical issue for aerodynamic development engineers. Starting from these considerations, the objective of this research is therefore, for varying upstream flow conditions, to use active flow control in order to maintain the drag performance at zero yaw angle carefully achieved during the optimization procedure. More specifically, in this work the primary focus is the control of the wake, as it has a predominant role in contributing to the overall pressure drag.

This study is performed using an academic, but representative, model at reduced scale called "Windsor model" (Good and Garry 14) used in numerous experimental and CFD studies. An on-road test campaign was also performed in windy conditions, capturing time-dependent data for resultant air speed, yaw angle, and base pressure distribution using car mounted instrumentation. Usual probability density functions (pdf) of yaw angles (β) were obtained with typically $-5° \leq \beta \leq 5°$ for 95% of the time. The main message from these campaigns is that large scale vertical or horizontal motions of the near wake are indeed detected and are main contributors to the variance of the base pressure fluctuation. Interestingly, low frequency global wake motions have a major contribution in real situations, which makes it interesting to search for quasi-steady active control approaches because the time scale of the external forcing of the wake by the slow external perturbations is then much larger than the advective time scale driving unsteady aerodynamic responses. For the road tests conducted on the Stellantis vehicle, 49 unsteady pressure sensors were installed on the base, allowing simultaneous data acquisition. A Proper Orthogonal Decomposition (POD) of the pressure data reveals that the two primary modes correspond to vertical and horizontal wake motion, collectively contributing to over 60% of the total variance in pressure fluctuations. Further spectral analysis of the random coefficients associated with these modes indicates that low frequencies (typically $St \leq 10^{-1}$) contribute more than 60% of the variance for these large-scale motions (Cembalo 2024). Given these findings, our approach in this study is to explore a quasi-steady control methodology.

We propose here an active solution for drag reduction consisting in controlling four rigid flaps positioned at the base of the vehicle. By employing the flaps, our goal is to manipulate the near wake orientation in order to maintain a reference pressure distribution at the base of the model. More precisely, the system output is based on four static pressure sensors only, located on the base of the model, used to represent a mean pressure level and the horizontal and vertical pressure gradients. The instrumented Windsor body (fig.1) has model wheels and is equipped with four controlled flaps at the rear. Wind tunnel tests are conducted to generate quasi-steady disturbances. Our results demonstrate that this complex system can be effectively modelled by a low-order Linear Time-Varying (LTV) model, with parameters predominantly varying based on the upstream flow properties. Our proposal involves the online identification of this black-box discrete time LTV model derived from experimental data. In addressing both the constraints imposed by flap angle saturation and the absence of state measurements, we developed a Recursive Subspace-based Predictive Control (RSPC) approach. In the closed-loop system, input/output data are intricately correlated with noise, and we propose an unbiased recursive estimator to mitigate these challenges. This approach ensures that the proposed solution remains economically viable, aligning with the industrial feasibility criteria. The latter offers the advantage of recursive estimation, allowing the control system to continuously update and refine its model based on real-time measurements. This adaptive capability enhances the robustness and accuracy of the control process, ensuring consistent performance over time and maximizing the drag reduction over the wide range of operating conditions. Subsequent closed-loop tests were carried out in the wind tunnel, demonstrating the viability and effectiveness of our approach. Two control objectives were tested. One consists in sustaining the basic pressure distribution having a lateral symmetry at zero yaw (fig. 2). The other one, more stringent, forces both vertical and horizontal symmetry of the distribution, along with a higher pressure level (fig. 3 and 4). In both cases, the control maintains efficiently the reference pressure distribution for quasi-steady yaw angle variations

representative of real driving situations. Subsequent analysis confirms a notable decrease in the base pressure coefficient C_b and, consequently, a reduction of the drag.

These promising outcomes validate the proof of concept, signifying a significant milestone. Nonetheless, substantial efforts lie ahead before implementation in production cars becomes feasible. The principal area for further improvement revolves around the actuators. Integrating active flaps in vehicles is not a practical solution. Conversely, exploring flexible tapers with the capability to deform locally the bodywork appears feasible. The efficacy of these actuators in precisely controlling the pressure at the rear of vehicles having a more complex rear geometry is yet to be substantiated. This is the subject of an ongoing research work.

REFERENCES

Jeff Howell, David Forbes, and Martin Passmore. A drag coefficient for application to the wltp driving cycle. Proceedings of the Institution of Mechanical Engineers, Part D: Journal of Automobile Engineering, 231(9):1274–1286, 2017. doi:10.1177/0954407017704784.

G. Le Good and K. P. Garry. On the use of reference models in automotive aerodynamics. SAE Technical Paper 2004-01-1308, 2004.

A. Cembalo. Amélioration de l'efficacité énergétique des voitures : Contrôle actif de la traînée aérodynamique en conditions amont variables. PhD thesis, Ecole Nationale Supérieure de Mécanique et d'Aérotechnique, 2024.

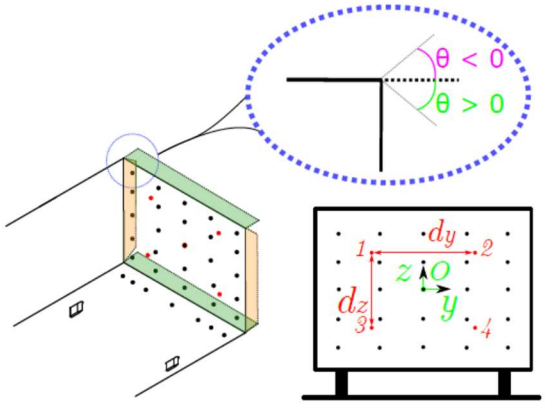

Figure 1: Control system. In orange and green the four rigid flaps, θ being the flap's displacement. The red pressure taps are the ones used for the system's outputs

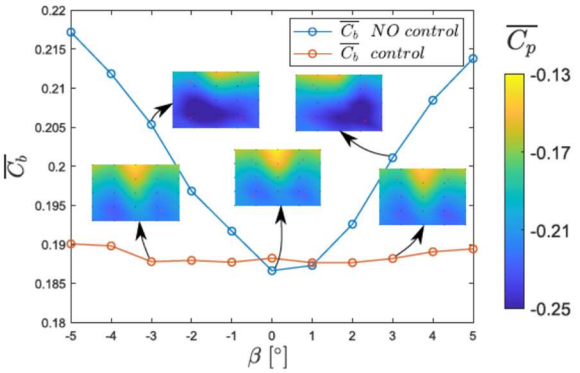

Figure 2: Mean value of the base pressure C_b versus β with lateral symmetry control (orange line) and without control (blue line). The standard deviation of C_b is about 2% of $\overline{C_b}$ in all depicted cases.

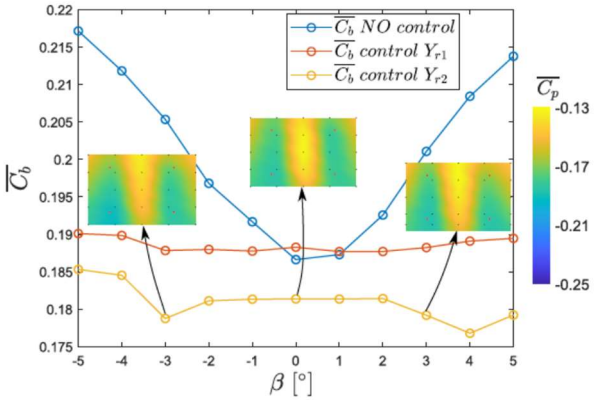

Figure 3: Mean value of the base pressure C_b versus β with symmetry control (yellow line) lateral symmetry control (orange line) and without control (blue line). The standard deviation of C_b is about 2% of $\overline{C_b}$ in all depicted cases.

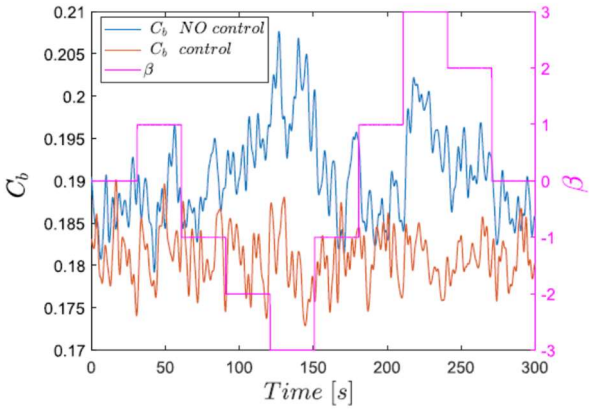

Figure 4: Mean base pressure C_b versus time in response to step variations of β. The pink line illustrates step changes, while the orange line represents the scenario with symmetry control, and the blue line depicts the scenario without control.

Optimised drag configurations of an Ahmed body in crossflow with top and bottom rear morphing spoilers allowing twisted deformations

Yajun Fan[*] and Olivier Cadot[†]

For ground vehicles aerodynamic, fundamental research on simplified 3D bluff bodies identified the main source of the drag as the low pressure at the base due to the massive separation at the trailing edge[1]. Numerous passive flow control techniques have been devised to achieve drag reduction, including tapers at the trailing edge, boat tailing, static flaps, and base cavities. However, these strategies, optimized for a wind-aligned attitude, may experience a loss of efficiency when the body attitude (yaw and pitch) undergoes changes. Thus, It is necessary to develop an adjustable control technique to achieve drag reduction under an arbitrary body attitude. The current work proposes morphing spoilers to reduce the aerodynamic drag of an Ahmed body. The morphing allows twisted deformation that will be shown to improve the drag reduction in crossflow conditions.

The considered geometry is a flat-back Ahmed model (see in Fig.1) with dimensions $L = 560$ *mm*, $W = 180$ *mm*, and $H = 200$ *mm*. The body is supported by four cylinders of 15 *mm* in diameter, leaving a ground clearance $C = 30$ *mm*. The model is placed on a six-component force balance to measure the aerodynamic force f_x, f_y, f_z in the coordinates system ($\mathbf{e}_x$, $\mathbf{e}_y$, $\mathbf{e}_z$). There are 20 pressure taps, all located at the base in the space of the height $\frac{3}{5}H$ (see the blue dots in Fig.1*b*), to give an estimate of the drag contribution $C_{xb} = \frac{3}{5}C_b$ over the flat surface (grey region in Fig.1*b*). The assembly is mounted on a motorized rotation stage to control the yaw angle β. The experiment is conducted in a blow-down wind tunnel under the free-stream velocity $U_\infty = 16.2 m/s$ (i.e. the dynamic pressure $q_\infty = 160$ Pa), corresponding to the Reynolds number $Re = U_\infty H/\nu \approx 2.2 \times 10^5$. The height of the body H and the free-stream velocity U_∞ are chosen as length and velocity scaling units respectively. The after-body is equipped with two morphing spoiler modules (see Fig.1*d*) at the top and bottom trailing edge. Two angles on both sides can be regulated independently, enabling either pure deflection or twisted deformation of the spoiler surface (see Fig.1*d*).

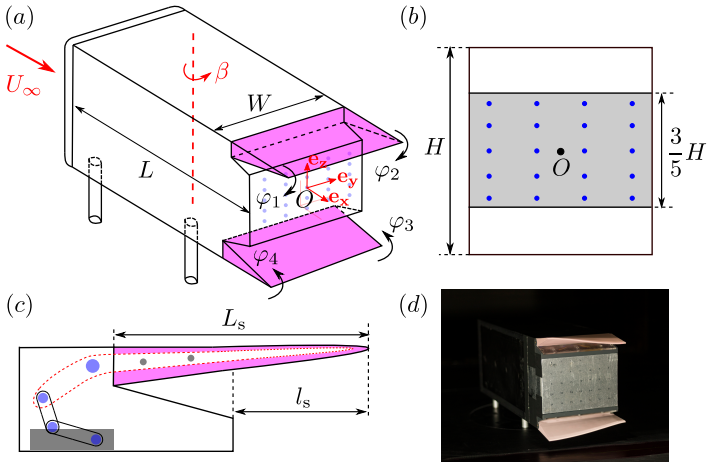

Figure 1: Sketch (*a*) of the geometry with two morphing spoiler. Rear (*c*) view showing the pressure taps location on the base. Sketch of (*c*) the morphing spoiler. Picture (*d*) showing a twisted spoilers configuration.

In the current work, three different spoilers configurations are investigated: the flat one $\varphi^{\text{flat}} = (0°, 0°, 0°, 0°)$, the reference one $\varphi^{\text{Ref}} = (10°, 10°, 6°, 6°)$ for which drag is minimal at null-yaw attitude and the optimal one $\varphi^{\text{opt}}_\beta$ obtained with the genetic algorithm at arbitrary yaw attitude β. As shown in Fig.2(*a*), the drag reduction

[*]University of Liverpool, Liverpool L69 BX7, United Kingdom
[†]University of Liverpool, Liverpool L69 BX7, United Kingdom
[1]Hucho and Sovran *Annu. Rev. Fluid Mech.* **25** (1993)

capability of the reference configuration is confined to a very small yaw range ($\beta < 2°$). Yawing the body is detrimental to the drag reduction effectiveness of the reference configuration, to the extent that it even increases the drag at a large yaw range ($\beta \geq 4°$) compared to the flat spoilers configuration. This is attributed to the diminished capacity to recover the base pressure through the reference spoiler (see in Fig.2*b*) and to the drag contribution of the spoilers themselves[2], as the yaw angle increases.The optimal spoilers achieve in average a drag reduction of about 7% compared to the reference spoilers for arbitrary yaw attitude. Fig.2(*c*) presents the variation of the optimal spoilers angles with the increase of the yaw. A twisting deformation is necessary to reduce the drag, especially for the bottom spoiler.

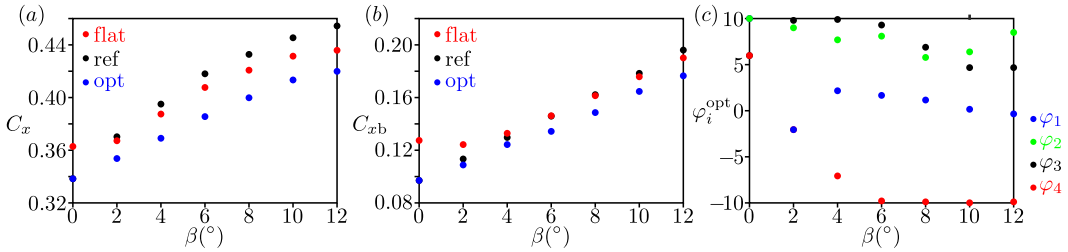

Figure 2: The variation of the drag C_x (*a*) and base drag C_{xb} (*b*) over the flat surface vs. yaw angle β for the flat spoiler, the reference spoiler and the optimal spoilers (see its variation with the yaw in *c*).

Fig.3 presents the mean velocity field and the turbulent kinetic energy in the cross-section at $x = 0.5H$ for a yaw $\beta = 6°$. The optimal spoilers configuration modifies the pronounced wake asymmetry in the horizontal direction to asymmetry in the vertical direction. It needs to be understood why drag reduction is associated with the transfer of the side force created by the wake towards the lift component. In addition, the reference spoilers configuration significantly enhances the wake fluctuation on the windward side compared to the flat spoilers. This could explain why, despite the thinning of the recirculating region, the base drag fails to decrease. While through spoilers shape optimization, the weakening of wake fluctuation is evident, thereby likely to also contribute to the recovery of base pressure.

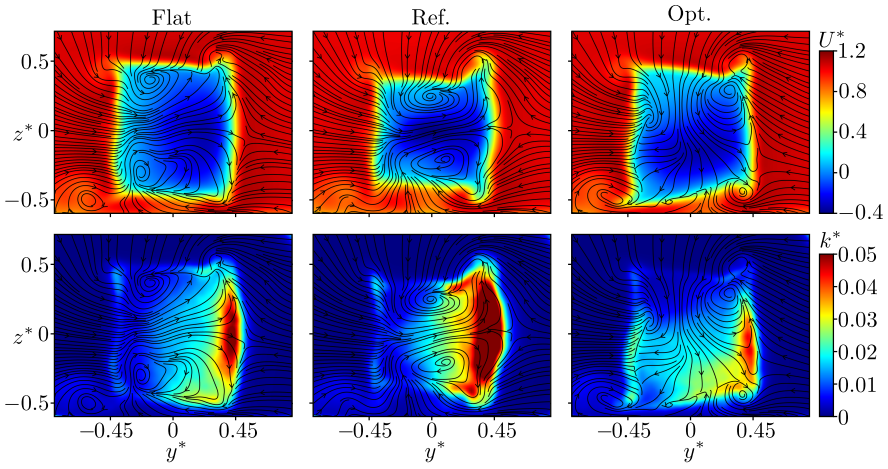

Figure 3: Mean velocity field (top row) and turbulent kinetic energy (bottom row) in the cross-plane $x^* = 0.5H$ for three spoiler configurations: (*a*) flat spoiler; (*b*) reference spoiler; (*c*) optimal spoiler at $\beta = 6°$.

In summary, this work investigated the effect on drag of spoilers shape at the trailing edge of a squareback Ahmed body in cross-flow conditions. The spoilers design, optimized under null-yaw conditions, experiences a loss in drag reduction with yaw and even exhibits an increase in drag at larger yaw angles. For these yaws, optimal deformation are twisted spoilers altering the wake orientation and attenuating the wake fluctuation.

[2]Fan et al. *Exp. Fluids* **65** (2024)

Reconstruction of turbulent bluff body wake using Physics Informed Neural Networks

Yusuf Patel*, Jonathan Morrison and Georgios Rigas

Department of Aeronautics, Imperial College London, UK
*E-mail: yusuf.patel15@imperial.ac.uk

Motivation: Accurate simulation of fluid flows (governed by the unsteady Navier-Stokes) using high fidelity methodologies is often intractable for turbulent regimes. Whilst solving the mean flow Reynolds-Averaged Navier-Stokes is computationally cheaper, they are less accurate, due to a lack of exact turbulence closure. Likewise, high-fidelity experimental data can be produced, but is often limited by practical constraints. Data assimilation techniques have been successfully used to combine high fidelity data with existing numerical methods to reconstruct fluid flows [1, 2]. In this work, we solve the inverse problem, to reconstruct a bluff body wake at $Re_D = 200000$ (see Figure 1 combining sparse experimental flow measurements and under-determined governing flow equations.

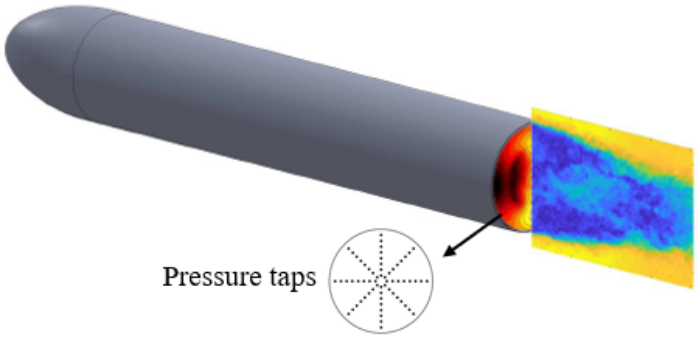

Figure 1: Experimental set up of bluff body wake at $Re_D = 200000$ showing instantaneous PIV velocity field and pressure tap locationsx.

Approach & Methods: This work will investigate how Physics-Informed Neural Networks (PINNs) (as seen in Figure 2) can be used to reconstruct the experimental bluff body wake. Depending on the formulation of the problem, we show how coarse velocity measurements can be super-resolved and how velocity fields can be used to infer the unknown pressure fields and vice versa.

In particular, we evaluate the effect of constraining PINNs with different formulations of the governing fluid equations and how this affects flow reconstruction accuracy. We examine use of i) the RANS equations without turbulence closure (PINN-Baseline) ii) the RANS equations with turbulence closure (PINN-SA) iii) the Harmonic-Balanced Navier-Stokes equations (PINN-HBNS). To this aim, we set up a constrained optimisation to find the flow solution, which minimises error to measurements J,

$$J = \sum_{m=1}^{N_m} ||\hat{\mathbf{u}}_\mathbf{m} - \hat{\mathbf{u}}_{\mathbf{m},\text{pred}}||^2 , \tag{1}$$

whilst obeying the governing equations. Furthermore, in this work, experimental data is used with PINNs (unlike in [1, 2]), and thus the effects of this must also be considered.

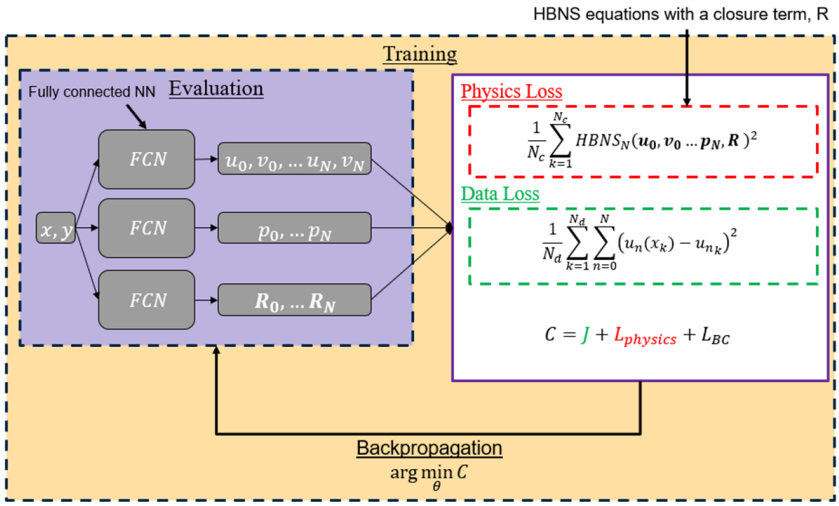

Figure 2: Structure of the Physics-Informed Neural Network. The deep neural network, denoted by N, produces a continuous solution for the flow as a function of location, defined by a set of weights and biases, θ. This enables the super-resolution of the velocity field.

Main findings: In this work, we show that the all proposed PINN formulations are able to successfully reconstruct a three-dimensional bluff body wake, from a single plane of sparse 2D2C, experimental PIV velocity data measurements, across a range of data resolutions. However, comparing the different PINN formulations highlight the differences between them. However, the addition of physics constraints (PINN-SA or PINN-HBNS) has a significant effect on flow reconstruction accuracy. Furthermore, small measurement errors found in experimental data presented new challenges that we will be adressing.

References

[1] L Sliwinski and G Rigas. Mean flow reconstruction of unsteady flows using Physics-Informed Neural Networks. *Data-Centric Eng.*, 2021:1–18, 2022.

[2] Y Patel, V Mons, O Marquet, and G Rigas. Turbulence model augmented physics-informed neural networks for mean-flow reconstruction. *Phys. Rev. Fluids*, 9:034605, Mar 2024.

Attitude effect on the stable and unstable recirculating flow of a blunt rectangular trailing edge body with wall proximity

Olivier Cadot [*], Yajun Fan[†]

We are investigating experimentally the flow past the bluff body shown in Fig. 1 at Re= 2×10^5 with the aim to address fundamental aspects of vehicle aerodynamics in the transportation industry. The study focuses on the wide recirculating region produced by the rear separation and the associated wake, leading to high drag and additional force when the body attitude defined by pitch α and yaw β is increased[1]. The study is repeated with a base cavity (inward translation of the base) presenting identical location of the rear separation. The base cavity is known to suppress the steady instability, responsible for the opposite vertical asymmetries in Fig. 1(left) at $\beta = 0^\circ$. In these velocity fields, the presence of the 2 spirals inside the recirculation delimited with the red line indicates an intersection with a skewed recirculating torus as sketched in the top left of Fig. 1. At an identical attitude, the base cavity present a straight recirculating torus as similarly sketched in Fig. 1. We thus investigate how the rear flow orientates for both cases with body attitudes within the range $-2.5^\circ < \alpha < 2.5^\circ$ and $0^\circ < \beta < 12^\circ$. At the conference, we will discuss how the recirculating torus, either stable or unstable deforms with the body attitude and how it affects the body aerodynamics.

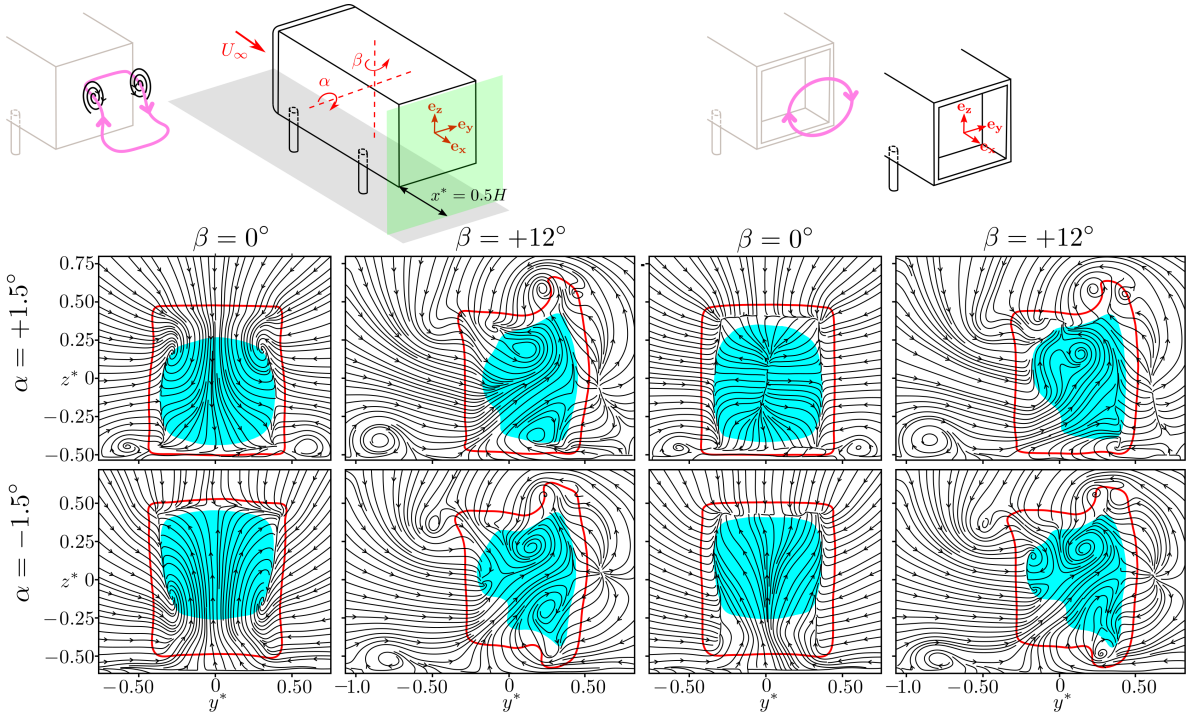

Figure 1: Mean velocity field in a fixed plane perpendicular to U_∞ showing a crossflow section of the recirculating bubble for 4 body attitudes for (left) flat base and (right) base cavity. Streamlines are made from the crossflow velocity components V, W. The feedback flow $U < 0$ is shown as the cyan area and the boundary of the separation is delimited by the red isoline $U = 0.625U_\infty$.

[*]University of Liverpool, Liverpool L69 BX7, United Kingdom
[†]University of Liverpool, Liverpool L69 BX7, United Kingdom
[1]Fan, Parezanović and Cadot, *J. Fluid Mech.* **942** (2022)